Observing Waterlogging and its Impact on Agriculture in Hungary Using Radar and Optical Images

ASHFAK MAHMUD
June 2022

SUPERVISORS:
Dr. Zoltán Vekerdy
Ir. Arno van Lieshout

ADVISORS:
Nadja den Besten
Dr. Ir. Anton Vrieling

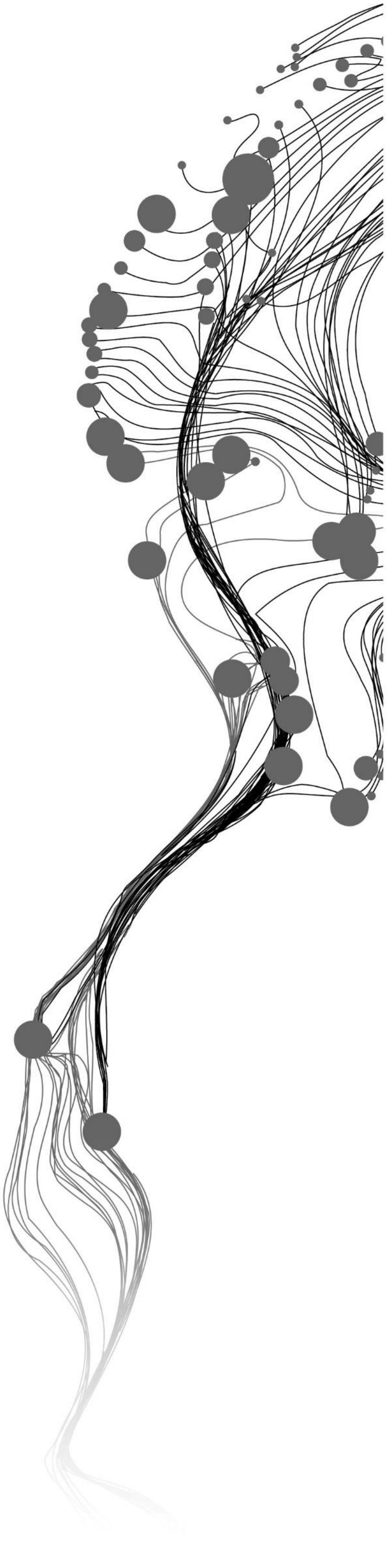

Observing Waterlogging and its Impact on Agriculture in Hungary Using Radar and Optical Images

ASHFAK MAHMUD
Enschede, The Netherlands, June 2022

Thesis submitted to the Faculty of Geo-Information Science and Earth Observation of the University of Twente in partial fulfilment of the requirements for the degree of Master of Science in Geo-information Science and Earth Observation.

Specialization: Water Resource and Environment Management

SUPERVISORS:
Dr. Zoltán Vekerdy
Ir. Arno van Lieshout

ADVISORS:
Nadja den Besten
Dr. Ir. Anton Vrieling

THESIS ASSESSMENT BOARD:
Dr. Maciek Lubczynski (Chair)
Dr. Boudewijn van Leeuwen (External Examiner, University of Szeged)

ABSTRACT

The study aims to detect waterlogging dynamics in agricultural fields and quantify its effect on crop development at different growth stages using synthetic-aperture radar (SAR) and optical satellite images. Firstly, waterlogging dynamics (occurrence, extent, and timing) have been detected from Sentinel-1 (S1) and PlanetScope (PS) images. Hereafter, temporal profiles from Sentinel-1(S1) and Sentinel-2 (S2) have been used to understand the development of the crop in different growth stages. Finally, the impact of waterlogging has been quantified by comparing crop development in non-waterlogged (NWL) and waterlogged (WL) locations in different growth stages by the synergistic use of radar (S1) and optical (S2) images.

A threshold value of Normalized Difference Water Index (NDWI) ≥ -0.27 on PS images was applied, and a threshold value of $\sigma^0_{VV} \leq$ -16 dB on S1 images was employed to separate the waterlogged areas. Temporal profiles of σ^0_{VH}, σ^0_{VV}, cross-ratio (CR), and radar vegetation index (RVI) from S1 and Normalized Difference Vegetation Index (NDVI) from S2 have been generated for the season 2021 to observe crop development. Time series analysis from sample sites at the intra-field level has been done to see how the crop development is reflected in NWL and WL crops. Finally, patterns of NDVI deviation in NWL and WL locations are mapped at the intra-field level in different growth stages.

Results show that PS detected 3.95% (7.17 km^2), where S1 spotted 3.76 % (6.83 km^2) of the area as waterlogging. CR and RVI from S1 and NDVI from S2 perform as a similar indicators of crop development monitoring. However, S2-derived NDVI shows an early increase and decrease than CR and RVI from S1 in the initial and senescence stages as NDVI is sensitive to chlorophyll, whereas CR and RVI are sensitive to biomass and vegetation water content (VWC). The highest NDVI differences (up to 0.4) between NWL and WL crops are noticed during the flowering and fruit development stage (May to mid-June). Due to less biomass being developed in the WL crop during leaf development and stem elongation stage in April, CR shows slightly lower values (2-3 dB) in WL locations. Similar to NDVI, the highest difference in CR and RVI between WL and NWL locations is found during May, when winter wheat shows maximum growth. A delay in crop growth in the WL location is also noticeable during crop development. The highest discrepancies between NWL and WL locations are found from January to March by combining S2-derived NDVI, and S1-derived scaled CR due to the sensitivity difference of NDVI and CR to waterlogging. From the leaf development and stem elongation to flowering and fruit development stages, the ratio of CR and NDVI responded similarly to crop growth in both waterlogging states. However, some inconsistencies are found during senescence due to the difference in the rate of biomass and chlorophyll loss in NWL and WL crops. The spatial patterns of NDVI deviation show that high and very high deviations coincide with the WL locations, especially when waterlogging has a longer duration, and the deviation is the highest during the flowering and fruit development stage. The study reveals that the synergy capabilities of optical and radar images are the potential for detecting waterlogging dynamics as well as assessing the difference in crop development between WL and NWL crops.

Keywords: Waterlogging, Sentinel 1, Sentinel 2, PlanetScope, Crop growth stages, NDVI, RVI, Cross ratio, winter wheat, time series analysis.

ACKNOWLEDGEMENTS

I would like to express my gratitude to the Faculty of Geoinformation Science and Earth Observation (ITC), the University of Twente, for granting me the ITC Excellence Scholarship to pursue my MSc degree. I also extend my gratitude to Faculty ITC for funding my fieldwork in Hungary.

I am deeply thankful to my supervisor Dr. Zoltán Vekerdy for his valuable time, guidance, encouragement, and suggestions throughout the research. Professor, 'köszönöm' for making me think deeply and providing me with valuable knowledge of remote sensing and physical environmental interactions. I am grateful for your words- "Ashfak, I am squeezing you so that you can pick raisins out of the cake" which encouraged me to try new things. Many thanks to you for driving around agricultural fields in Szarvas and Mezőhegyes in Hungary with your car. I am also thankful to my second supervisor Ir. Arno van Lieshout for always having my back and his valuable feedback to improve the thesis. I would like to acknowledge the help from Florent and Yohannes during my fieldwork in Hungary.

I want to thank Richard de Jeu and Nadja den Besten for giving me the opportunity to do my master's thesis with Planet. I learned a lot from the Planeteers, especially from the biomass proxy team. Nadja, I would like to thank you for your constant support and supervision every week. Thank you again for keeping me on track and pushing me to learn and apply Python coding in my work. I enjoyed working with you and we both make a good team.

I am forever indebted to my parents and elder brothers for their endless support, belief, and love. I can not thank enough my father who always believed in me in every situation and encouraged me to pursue higher study in a foreign country. I would like to thank my cousin Sheikh Mohammed Belal and his wife Dr. Dilruba Nasrin for making the Netherlands my second home. I would never forget their support and homely love from the beginning. Last but not least, I would like to thank Trisha for being an unconditional listener and supporter during the time of stress and challenge.

Ashfak Mahmud
June 2022
Enschede, the Netherlands

TABLE OF CONTENTS

1. Introduction 8
    1.1. Background and research problem 8
    1.2. Research objectives and research questions 9
2. State of the Research 10
    2.1. Review of the use of SAR data in observing waterlogging in agricultural areas 10
    2.2. Review of the use of passive microwaves in observing waterlogging in agricultural areas 11
    2.3. Review of optical data in observing waterlogging in agricultural areas 12
3. Study Area 13
    3.1. Study site 13
    3.2. Climate 13
    3.3. Landcover and landuse 14
    3.4. Soil characteristics 14
    3.5. Topography 15
    3.6. Field visit and reconnaissance 15
4. Datasets 19
    4.1. Satellite data 19
    4.2. Agroclimatic data 21
    4.3. Soil moisture 21
    4.4. Crop growth stages 21
5. Research Methods 23
    5.1. Waterlogging detection 23
    5.2. Combination of optical and radar waterlogging map 26
    5.3. Time series analysis 26
    5.4. Mapping spatial patterns of NDVI deviation in NWL and WL locations 28
6. Results and Discussion 29
    6.1. Agroclimatic factors 29
    6.2. Mapping waterlogging dynamics 30
    6.3. Time series analysis and crop development monitoring 35
    6.4. Variability of satellite data in WL and NWL fields 37
    6.5. Mapping spatial patterns of NDVI deviation in NWL and WL locations 45
7. Conclusions and Recommendations 47
    7.1. Conclusion 47
    7.2. Limitations and recommendations 50
8. Reference 51

LIST OF FIGURES

Figure 1: Radar backscattering mechanism in WL agricultural land: a) diffuse scattering on the rough surface, b) double bounce, c) specular reflection on the smooth water surface, d) diffuse volume scattering on the canopy. 10

Figure 2: Time series of soil moisture derived from SMAP L-band passive microwave observation for irrigated and non-irrigated sugarcane plantation (den Besten et al., 2021). 12

Figure 3: Study area location around Szarvas, Hungary. The orange blocks indicate winter wheat parcels (n=22), and the green points are test locations. 13

Figure 4: Annual precipitation and area covered with waterlogging in Hungary from 1935 to 2011 (Pálfai, 2011). 14

Figure 5: Landcover map (10m) of Békés county from European Space Agency (ESA) WorldCover of 2020. The black box indicates the study area, Szarvas. 14

Figure 6: Soil texture map of Hungary [adopted from Mez˝ Osi et al. (2015) based on AGROTOPO.] The red box indicates the study area. 15

Figure 7: Digital elevation model of the study area [source: EU-DEM, (2017)]. 15

Figure 8: S1 descending (left) and ascending (right) passes in different relative orbital tracks covering the study area. The red box shows the study area in Hungary (gray shade). 19

Figure 9: S2 tiles covering the study area. The red box indicates the study area in Hungary (gray shade). 20

Figure 10: S1 and cloud-free S2 temporal coverage in the year 2021 over the study area. The collections include observations from all orbits. 20

Figure 11: PS waterlogging mapping process. 24

Figure 12: S1 waterlogging mapping process. 25

Figure 13: Evaluation of different speckle filtering methods to detect waterlogging. The red circle in median filtering indicates a small WL place which is cleared out in other filtering options. 25

Figure 14: Sensitivity analysis of different NDWI and VV backscatter threshold values over PS and S1 images, respectively, in detecting waterlogging. The red dash lines indicate the selected threshold and corresponding WL areas for the study. 26

Figure 15: Smoothening of CR from S1 using rolling mean (green line) and Savitzky–Golay (gray line). 27

Figure 16: NDVI deviation mapping process. 28

Figure 17: Precipitation [$mm\ d-1$] (top), SWC [$m3m-3$] (middle) and temperature [°C] (bottom) data in Szarvas, Hungary. 29

Figure 18: Spatial distribution waterlogging extent and occurrence detected from PS images in Szarvas, Hungary. 30

Figure 19: Spatial distribution waterlogging extent and occurrence detected from S1 images in Szarvas, Hungary. 31

Figure 20: Comparison of the waterlogging maps from S1 and PS. 32

Figure 21: Waterlogging extent and observed water frequency detected from combined S1 and PS observations in Szarvas, Hungary. 33

Figure 22: Scatterplot of mean VV backscatter (left) and VH backscatter (right) between WL and NWL areas. 34

Figure 23: Time series of S1 VV backscatter (dB) in WL (blue) and NWL (green) areas within the same parcels. 34

Figure 24: Temporal profile of S2 NDVI for all wheat parcels (n=22) in Szarvas, Hungary. 35

Figure 25: Temporal profile of S1 backscatter data for all wheat parcels (n=22) in Szarvas, Hungary; (top) VH backscatter (dB) and (bottom) VV backscatter (dB). 36

Figure 26: Temporal profile of S1 (top) CR (dB) and (bottom) RVI for all wheat parcels (n=22) in Szarvas, Hungary. 37

Figure 27: Time series of S1 VH backscatter and VV backscatter in WL and NWL locations in wheat fields in Szarvas, Hungary. 38

Figure 28: Time series of S1 CR and S2 NDVI in WL and NWL locations in different wheat fields in Szarvas, Hungary. 39

Figure 29: Time series of S1 RVI and S2 NDVI in WL and NWL locations in different wheat fields in Szarvas, Hungary. 40

Figure 30: Correlogram between mean CR, NDVI, RVI, VH and VV backscatter where the color indicates the state of waterlogging. The green color is NWL, and the orange color is WL locations. 41

Figure 31: Pearson correlation coefficients between mean CR, NDVI, VH and VV backscatter in (A) NWL and (B) WL locations. 42

Figure 32: Violin plot of the distribution of mean satellite responses in different crop growth stages in NWL and WL locations over the growing season of 2021. 43

Figure 33: Time series of the ratio of S1 CR (scaled) and S2 NDVI in different wheat fields in Szarvas, Hungary. 44

Figure 34: Mapping spatial patterns of NDVI deviation in NWL and WL winter wheat at different growth stages. 46

LIST OF TABLES

Table 1: Descriptions of the fieldwork sites. 16

Table 2: List of S1 GRD-IW data available over the study area. 19

Table 3: List of S2 data available over the study area. 20

Table 4: PS surface reflectance ortho tile image description (Planet Labs, 2022). 21

Table 5: Growth stages with the approximate length of winter wheat in Szarvas, Hungary. 22

Table 6: Equations used for calculating NDVI, CR and RVI. 26

Table 7: Statistics of waterlogging area. 31

ACRONYMS

BBCH	Biologische Bundesanstalt, Bundessortenamt und CHemische Industrie
CR	Cross Ratio
dB	Decibel
DEM	Digital Elevation Model
GEE	Google Earth Engine
GRD	Ground Range Detected
IW	Interferometric Wide
NDVI	Normalized Difference Vegetation Index
NDWI	Normalized Difference Water Index
NWL	Non-Waterlogged
PS	PlanetScope
RVI	Radar Vegetation Index
SAR	Synthetic-Aperture Radar
S1	Sentinel-1
S2	Sentinel-2
SWC	Soil Water Content
VH	Vertical Transmit, Horizontal Receive
VV	Vertical Transmit, Vertical Receive
VWC	Vegetation Water Content
WL	Waterlogged

1. INTRODUCTION

1.1. Background and research problem

Agriculture plays an important role in securing the sustainable food security of a country. However, adverse weather impacts, such as waterlogging, can reduce the productivity of agricultural lands. Waterlogging refers to the excess water in the soil pores and root zone that obstruct gas transfer between soil and the atmosphere (den Besten et al., 2021; Marti et al., 2015; Ritzema, 2016). Across the literature, different terms are used to refer waterlogging as inland excess water (Pásztor et al., 2015a; Van Leeuwen et al., 2020), ponding water (Pantaleoni et al., 2007), temporary flood (Tsyganskaya et al., 2018a).

Both natural and anthropogenic causes can be responsible for waterlogging. Waterlogging usually occurs naturally in flat-land due to substantial rainfall, groundwater contribution (Pásztor et al., 2015b), and soil impermeability (Ritzema et al., 2008). Moreover, local small-scale depressions and a shallow groundwater table increase the chance of having waterlogged (WL) soils (Valipour, 2014). On the other hand, poor drainage systems, excessive irrigation (Linkemer et al., 1998), and ridge tillage (Chen et al., 2020) are examples of human intervention that can result in waterlogging.

WL soils obstruct the gas exchange of the plants and hamper the transpiration and photosynthesis process of the plants (Sairam et al., 2008; Sasidharan & Voesenek, 2015). Agricultural damage happens when the plants cannot get sufficient oxygen due to high groundwater levels for an extended period (Karoly et al., 2013). Besides, stomatal opening is heavily affected when plant roots cannot uptake ions due to oxygen deficiency caused by WL soil (Irfan et al., 2010). Waterlogging affected plants exhibit wilting, yellowing leaves, and a reduction in the growth and yield of the crops (Kaur et al., 2020; Shaw et al., 2013). Excess water in agricultural areas negatively influences the development and growth of crops and crop productivity.

Depending on its duration, frequency, extent, and timing, waterlogging results in damage to the quality and quantity of the crops in the affected agricultural areas (Karoly et al., 2013). Agricultural practice, soil type, climate, crop type, variety, and age are some notable factors influencing the impact of waterlogging. To accurately assess the crop damage, parameters such as waterlogging timing, water depth, and flow velocity need to be considered (Tapia-Silva et al., 2011).

The classical method of waterlogging detection and crop damage assessment requires field visits and manual digitization of waterlogging and crop damaged areas which is a very time-consuming, labor-intensive, and costly task. Quick detection of waterlogging and damaged area is needed to support farmers' management practice. So timely and accurate waterlogging mapping and agricultural impact assessment with remote sensing are inevitable (Van Leeuwen & Tobak, 2015). Nowadays, earth observation data provides a rapid and cost-effective solution for water detection (Nasirzadehdizaji et al., 2019), mapping crops (Mosleh et al., 2015), and monitoring crop conditions (Yu et al., 2013). Continuous crop monitoring throughout the season can give an overview of the alteration due to waterlogging. Since intensive rainfall is one of the reasons for triggering waterlogging, observation with optical sensors is problematic as cloudy situation prevails during the time of waterlogging (den Besten et al., 2021; Prigent et al., 2020). Moreover, the inability to observe under the canopy is the limitation of remote sensing techniques, especially for monitoring waterlogging in agricultural fields (den Besten et al., 2021; Lillesand et al., 2015).

So far, no research has been done on waterlogging and its impact on crops throughout the crop lifetime with the synergistic use of optical and radar images. Therefore, in this research, waterlogging occurrence, extent, and timing have been studied using very fine and moderate resolution PlanetScope (PS) and

Sentinel-1 (S1) images. Moreover, the impact of waterlogging on crops in different growing stages has been quantified utilizing the Sentinel-1 (S1) and Sentinel-2 (S2) time series. The results of the research will help the agronomist to understand the variation of the effects of waterlogging throughout the season. Moreover, the research outcomes will help the farmers to plan and optimize the management practice (e.g., improving drainage and replacing with waterlogging resistant variety or crops) to combat damage resulting from waterlogging.

An example of a country struggling with waterlogging is Hungary, where waterlogging is very dynamic, and more than 24% of the agricultural land is moderately or highly vulnerable to it (Mezősi, 2017). Since about 50% of the territory of Hungary is low-flat land, larger areas of the country are vulnerable to waterlogging (Kuti et al., 2006). Moreover, frequent temporary waterlogging has become a severe problem in the Hungarian Plain due to extreme and erratic rainfall in recent years. The large geographic extent of the endangered area makes it more difficult to predict its occurrence (Pálfai, 2011; Vízűgy, 2011). Throughout the study, agricultural fields in Szarvas, Hungary, have been used as a case study.

1.2. Research objectives and research questions

1.2.1. General objective

To detect waterlogging dynamics in agricultural fields and quantify its effect on crop development using Synthetic-Aperture Radar (SAR) and optical satellite images.

1.2.2. Specific objectives

The specific objectives with relevant research questions are:

Specific objective 1: To detect and map waterlogging dynamics (occurrence, extent, and timing) across the selected study area using S1 and PS images.

> **RQ1:** How can the waterlogging dynamics (occurrence, extent, and timing) be detected using S1 and PS images across the study area?
>
> **RQ2:** What are the differences and similarities between waterlogging dynamics detected from S1 and PS images?

Specific objective 2: To monitor crop development throughout the season by utilizing temporal profiles of S1 images (VV, VH, and VH/VV) and vegetation indices (e.g., RVI and NDVI) extracted from S1 and S2 images, respectively.

> **RQ3:** How can crop development be monitored with S1 and S2 images?
>
> **RQ4:** How do cross-ratio (CR = VH/VV), RVI, and NDVI derived from S1 and S2 vary in different crop growth stages?

Specific objective 3: To quantify the impact of waterlogging on crops by comparing crop development in waterlogged (WL) and non-waterlogged (NWL) locations in different crop growth stages.

> **RQ5:** What is the impact of waterlogging observed in different crop growth stages using the S1 and S2 time series?
>
> **RQ6:** How can the difference in crop development be evaluated in WL and NWL crops by combining S1 and S2?
>
> **RQ7:** What is the spatial pattern of NDVI deviation in NWL and WL locations in different growth stages at the intra-field level?

2. STATE OF THE RESEARCH

The following sections give an overview of the state of the research related to the most important aspects of observing waterlogging and its effects with microwave and optical techniques in agricultural areas.

2.1. Review of the use of SAR data in observing waterlogging in agricultural areas

Surface objects interact with the radar signals in a complex way. Therefore, many aspects of these interactions must be considered in detecting waterlogging and its effects in a complex agricultural environment.

2.1.1. Backscatter interaction

Radar backscatter depends on surface roughness and dielectric property of the scattering surface (Kim & Van Zyl, 2009). Backscatter from waterlogged vegetation (e.g., agricultural land) involves complex processes. Total captured backscatter from waterlogged vegetation includes scattering from the canopy, water, and soil surface. Standing smooth water surface in the waterlogged area creates specular reflection when radar signals are reflected away from the sensor resulting in low backscatter (Figure 1). Sometimes, backscatter increases as a result of double bounce scattering if the radiation hits between the water surface and vegetation stem perpendicularly and is reflected to the sensor (Pulvirenti et al., 2011; Pulvirenti et al., 2013; Woodhouse, 2006).

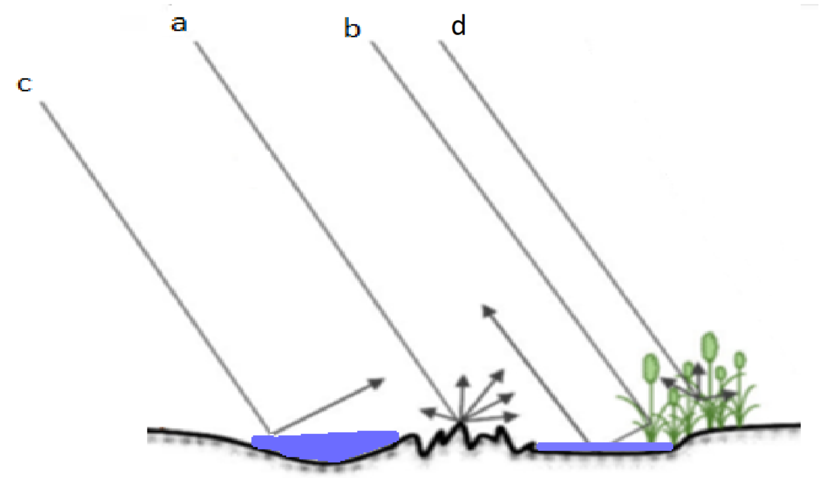

Figure 1: Radar backscattering mechanism in WL agricultural land: a) diffuse scattering on the rough surface, b) double bounce, c) specular reflection on the smooth water surface, d) diffuse volume scattering on the canopy.

2.1.2. Wavelength

Radar has a longer wavelength than the optical signals, which is capable of penetrating cloud. Depending on the ratio of the wavelength and the geometric parameters of the canopy (thickness and the size of the leaves and branches), water under the canopy can be observed (Hess et al., 2003; Wang, 2002). Studies suggested that the L band radiation with a wavelength of 15-30 cm is suitable for detecting waterlogging beneath the vegetation (Betbeder et al., 2014; Hess et al., 1995, 2003). The capability of penetrating vegetation becomes limited at shorter wavelengths, such as C-band (3.75-7.5 cm) and X-band (2.5- 3.75 cm) (Costa et al., 2002; Hess et al., 2003; Parker, 2010). Nevertheless, this capability depends on vegetation height, gap, and density. Generally, C-band and X-band are useful to detect waterlogging if the vegetation density is low or during the leaf-off (no foliage) condition (Martinis & Rieke, 2015; M. Zhang et al., 2016).

2.1.3. Polarization

Polarization in the SAR system can be horizontal (H) or vertical (V) in a single channel. The signals can be transmitted and received in co-polarised (VV or HH), cross-polarised (HV or VH), and dual-polarised modes (HH and VV, HH and HV, and VV and HV). Numerous studies suggested that HH is more suitable for detecting WL vegetation as double-bounce scattering is lower in VV than HH polarization (Wang et al., 1995). The HH polarization has a better monitor capability of the vegetation compared to VV, and HH is better reflected when hitting the water surface (Pierdicca et al., 2013). Furthermore, co-polarisation is better in detecting waterlogging as double-bounce scattering is more detectable in co-polarisation than cross-polarisation (Hess et al., 1990; Marti-Cardona et al., 2010).

Single-polarised images cannot differentiate different scattering mechanisms when looking into WL plants. However, backscatter intensity increases in inundated vegetation, making detection easy with proper knowledge of the area studied (Betbeder et al., 2014). Although in the past, Pulvirenti et al. (2011) and Kasischke et al. (2003) used single-polarised data to detect water in agricultural lands, nowadays, multi-polarised SAR data are popular as it can give more insight into detecting individual scattering mechanisms (Souza-Filho et al., 2011).

2.1.4. Incident Angle

In general, the incident angle of a satellite sensor ranges between 10° to 65°, steep to shallow. A steeper angle has a shorter path, enabling SAR signals to pass through the vegetation canopy more quickly than a shallow angle (Tsyganskaya et al., 2018b). Therefore, studies showed that a smaller incident angle is somewhat better for detecting waterlogged vegetation (Bourgeau-Chavez et al., 2009; Costa et al., 2002; Kandus et al., 2014; Richards et al., 2007). However, according to the results from Lang et al. (2008), the ability to detect waterlogged vegetation did not change much while changing the incident angle.

2.1.5. Biomass

Aboveground biomass has a significant influence on detecting WL areas under vegetation. Biomass is illustrated as canopy (Dwivedi et al., 1999), leaves, and stems (Kasischke et al., 2003). According to the studies by Mougin et al. (1999), Pope et al. (1997), Sang et al. (2014), and Yu et al. (2016), radar backscatter increases with the growth of biomass. For a given frequency, the saturation point, determined by biomass at which water is no longer detectable under vegetation, changes with the crop phenology.

2.1.6. Soil Moisture, water depth, and plant height

The backscattered signal from WL vegetation is also influenced by the physical characteristics of the ground surface contribution. Results from Kasischke et al. (2003) indicated that an increase in backscatter is noticeable if the soil moisture increases in all growth stages of the plants. However, only double-bounce and volume scattering from the canopy is dominant if the soil is WL (Kwoun & Lu, 2009).

According to the study from Pulvirenti, Chini et al. (2011), backscatter intensity is influenced by the water level in WL agricultural vegetation. Plant height and water level changes can show increased backscatter due to the predominant double-bounce effect when the plant is partially submerged in water. Nevertheless, backscatter will not increase at the beginning stage of the crop as short plant height does not introduce the double-bounce effect (Pulvirenti, Chini, et al., 2011).

2.2. Review of the use of passive microwaves in observing waterlogging in agricultural areas

According to numerous studies, the passive microwave has a great potential to detect waterlogging under dense vegetation (Choudhury, 1989; Hamilton et al., 1996; Prigent et al., 2001; Sippe et al., 1998a). The high dielectric constant of water compared to soil shows low emission of microwave signals, making waterlogging more detectable (Sippe et al., 1998b). Lower frequency (e.g., L-band) passive microwave signals are better than higher frequency (Ka-band) in detecting soil wetness under the canopy as the atmosphere and canopy have less influence on lower frequency signals. Den Besten et al. (2021) used L-band-derived soil moisture for monitoring soil moisture over sugarcane fields for irrigated and non-irrigated areas (Figure 2). However, the passive microwave has a limitation of coarse spatial resolution to detect waterlogging.

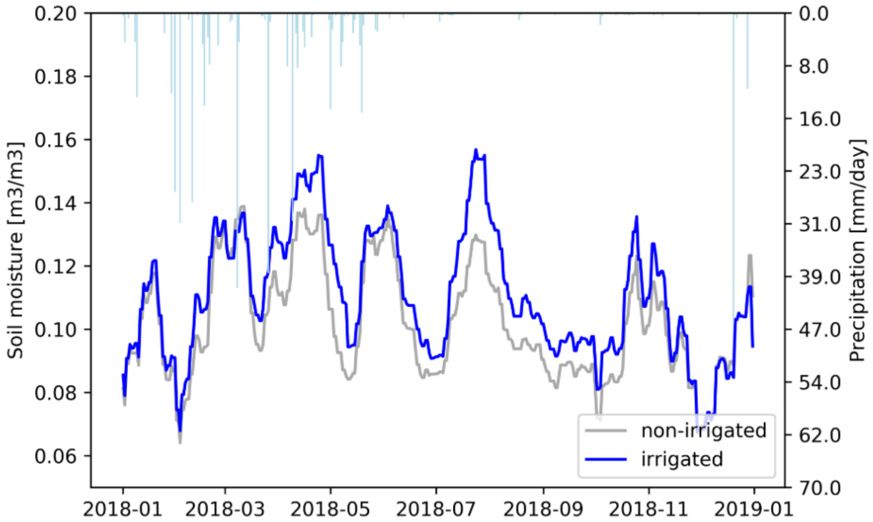

Figure 2: Time series of soil moisture derived from SMAP L-band passive microwave observation for irrigated and non-irrigated sugarcane plantation (den Besten et al., 2021).

2.3. Review of optical data in observing waterlogging in agricultural areas

Optical satellite images are capable of detecting waterlogging as water emits visible (VIS) and near-infrared (NIR) signals differently (den Besten et al., 2021). In general, water absorbs longer wavelengths, whereas short wavelengths are more reflected. For instance, the infra-red showed promising results in detecting WL areas (Choubey, 1997). Brahmabhatt et al. (2000) and Mandal & Sharma (2001) found that WL soil exhibited deep dark grey to light black color in the visual interpretation method. Chowdary et al. (2008) applied Normalized Difference Water Index (NDWI) to detect WL surfaces in rice, maize, and wheat fields. Furthermore enhanced vegetation index (EVI) and land surface temperature (LST) can be very useful for monitoring sub-surface WL agricultural land by analyzing the distinct ecology and thermodynamics of the WL plants (Xiao et al., 2014). Furthermore, den Besten et al. (2021) illustrated that the NDVI time series can be used to monitor waterlogging impact on crop growth. Pekel et al. (2016) successfully detected flooded irrigated rice paddies with JRC global surface water dataset in Sacramento Valley, USA, by analyzing Landsat imageries from 1984 to 2015.

3. STUDY AREA

The chapter includes descriptions of the study site, climate, land cover, and land use, soil characteristics, topography and field visit, and reconnaissance.

3.1. Study site

The study area is 180 km^2 and lies in the southeast part of the Great Hungary plain (Figure 3). The Körös river runs through the study site in the north-western part. According to the study by Van Leeuwen et al. (2017), the area is moderately to highly vulnerable to waterlogging.

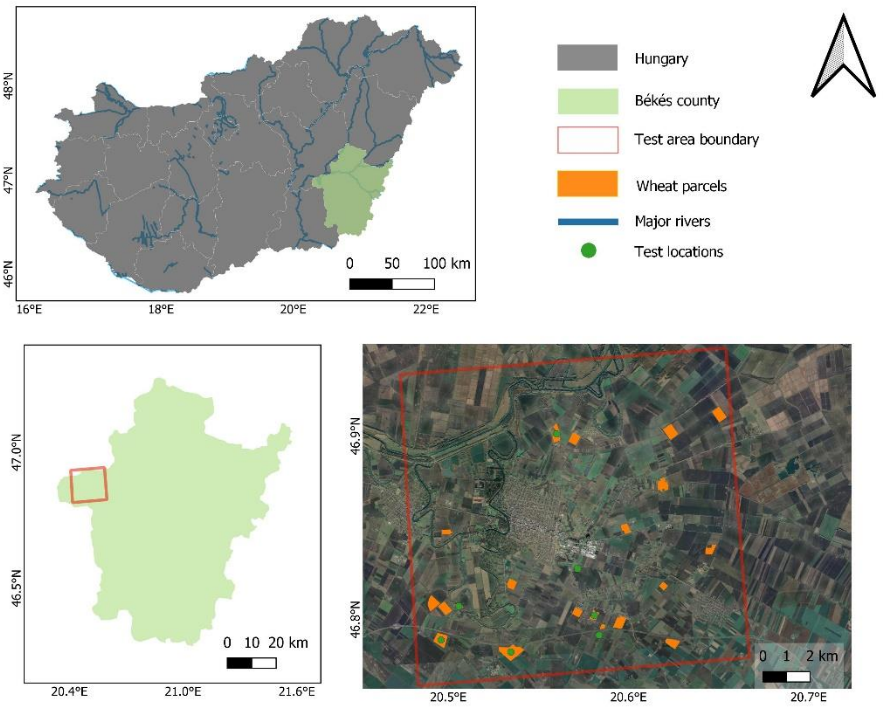

Figure 3: Study area location around Szarvas, Hungary. The orange blocks indicate winter wheat parcels (n=22), and the green points are test locations.

3.2. Climate

Hungary has a humid continental climate, and hot summer can be observed in many areas (Beck et al., 2018). The average temperature ranges from 8° to 11° with January and July being the coldest and hottest months respectively (Barreto et al., 2017) . Most rainfall falls from May to August, whereas potential evaporation is also high during this time. However, sudden high rainfall events and snowmelt, in combination with low evaporation, result in waterlogging between November and March (Yun, 2017). Figure 4 shows that more than 250,000 ha area in Hungary was found WL in 1999, 2000, 2006, and 2010 (Pálfai, 2011; Vízűgy, 2011).

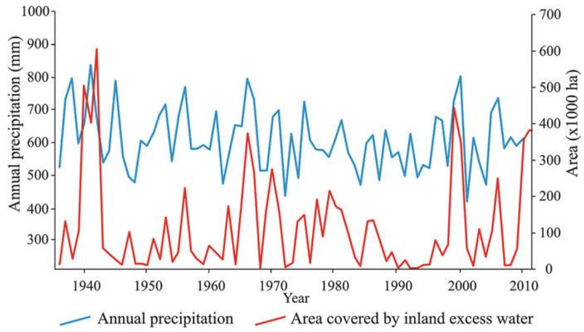

Figure 4: Annual precipitation and area covered with waterlogging in Hungary from 1935 to 2011 (Pálfai, 2011).

3.3. Landcover and landuse

Landcover in Békés county and Szarvas (Figure 5) is mainly dominated by cropland. The main crops produced in this area are winter wheat, alfalfa, maize, and rapeseed.

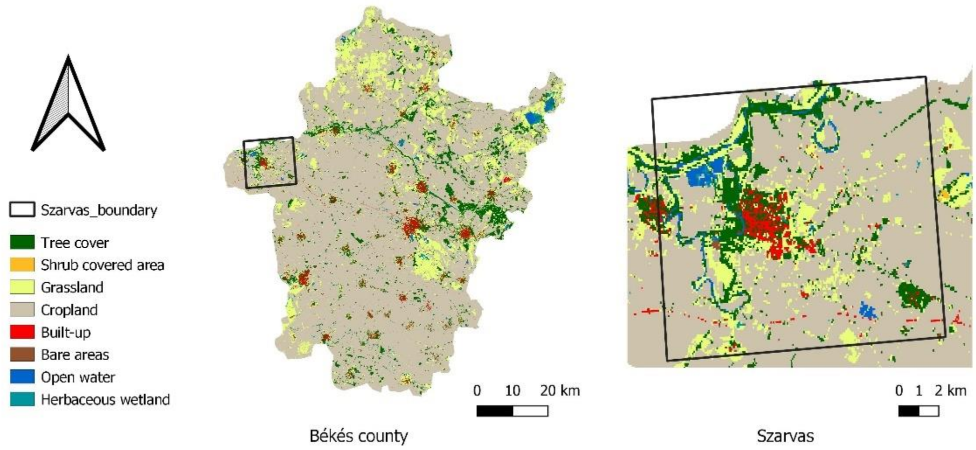

Figure 5: Landcover map (10m) of Békés county from European Space Agency (ESA) WorldCover of 2020. The black box indicates the study area, Szarvas.

3.4. Soil characteristics

The soil texture and grain size are vital indications of waterlogging (Karoly et al., 2013). The study area has clay loam and clay soil texture depicted in Figure 6. The hydrologic conductivity of loamy and clayey sediments varies between 2-45 mm/h and 0-4 mm/h, respectively, whereas for sand, it is 50-600 mm/h (Lajos, 2009). According to the results from Khadka (2018), clayey texture showed very less infiltration rate compared to other soil textures. Thus, the clayey soil is the most susceptible to the development of waterlogging. The study area has chemozems as the dominant soil type (Pásztor et al., 2018).

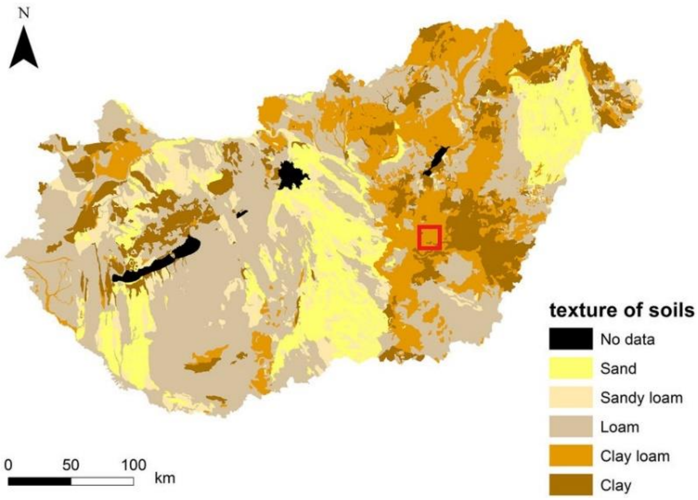

Figure 6: Soil texture map of Hungary [adopted from Mez˝ Osi et al. (2015) based on AGROTOPO.] The red box indicates the study area.

3.5. Topography

Figure 7 shows the Digital elevation model (DEM) of Hungary. The study area is located on the flat terrain of the Great Hungarian Plain. The study area has an elevation difference of only about 20 m, and the local relief may trigger (accumulated) waterlogging from rainfall events (Pásztor et al., 2006).

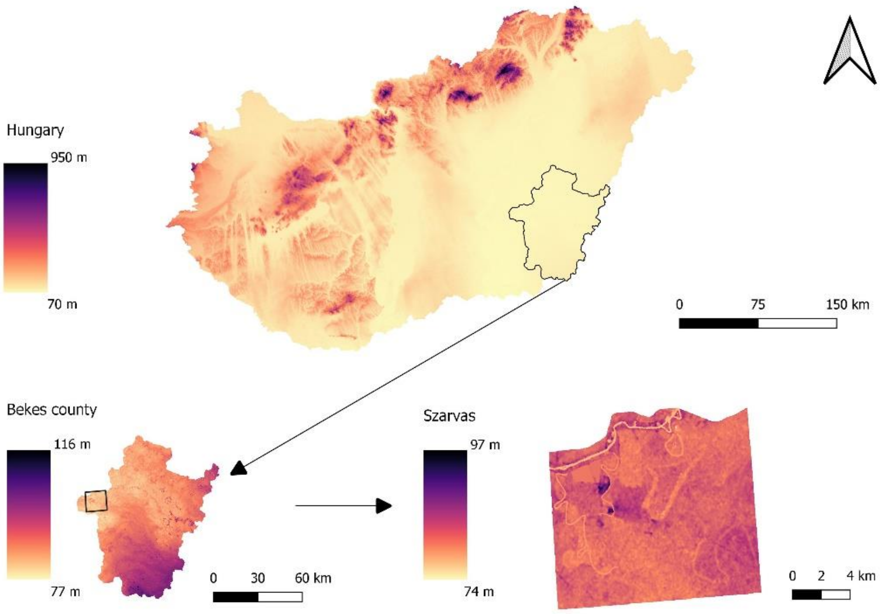

Figure 7: Digital elevation model of the study area [source: EU-DEM, (2017)].

3.6. Field visit and reconnaissance

A fieldwork was conducted from 12th March to 14th March in Szarvas, Hungary. Before going to the field, some selected plots with waterlogging vulnerability have been identified by visual inspection of Google Earth Pro imageries from the study period (2020-2021). Several time series analyses from S1 in selected WL and NWL areas have been checked prior to the field visit to understand the backscattering differences. The fieldwork started with a reconnaissance survey in different plots to understand the study area's land cover, topography, and agricultural practices. During the fieldwork, no waterlogging occurred as there was very low rainfall from January 2022 to March 2022. However, traces of waterlogging have been found in some plots, and the differences in soil roughness, texture, moisture content, and vegetation were noticeably different from unaffected areas. Areas with waterlogging traces were investigated with a hand auger down to 60-80 cm to see the soil profile and texture compared with areas with no traces of waterlogging. The descriptions and photographs of the visited fields are shown in Table 1.

Table 1: Descriptions of the fieldwork sites.

<table>
<tr><th colspan="2">Area 1a</th></tr>
<tr><td>Information</td><td>Date: 13th March 2022
Coordinate: 46°52'47.20"N, 20°30'8.79"E
Trace of waterlogging: yes
Description:
Covered with winter wheat of about 5-7 cm average in size.
Wheat plants are more sparse, yellowish, and shorter than the NWL part of the plot.
Clay at 50 cm, very much clayey, compact, and hard impermeable soil.
It was difficult to dig even with an auger because of its hardness.</td></tr>
<tr><td>Photographs</td><td>   </td></tr>
</table>

<table>
<tr><th colspan="2">Area 1b</th></tr>
<tr><td>Information</td><td>Date: 13th March 2022
Coordinate: 46°52'42.96"N, 20°30'10.59"E
Trace of waterlogging: no
Description:
Winter wheat plants have an average size of 7-10 cm.
Wheat plants are greener, longer, and more closely packed than WL plants.
The soil texture is less clayey than the WL part.
It was comparatively easier to dig the soil.</td></tr>
<tr><td>Photographs</td><td>  </td></tr>
</table>

<table>
<tr><th colspan="2">Area 2a</th></tr>
<tr><td>Information</td><td>Date: 14th March 2022
Coordinate: 46°48'47.15"N, 20°35'43.56"E
Trace of waterlogging: yes
Description:
Covered with winter wheat of about 5-6 cm in size.
Very low leaf development or dead plant due to waterlogging effect.
It had a canal to drain out excess water (see photographs).
Waterlogging traces were found in two spots within the same field.</td></tr>
<tr><td>Photographs</td><td>   </td></tr>
</table>

<table>
<tr><th colspan="2">Area 2b</th></tr>
<tr><td>Information</td><td>Date: 14th March 2022
Coordinate: 46°48'47.10"N, 20°35'43.35"E
Trace of waterlogging: yes
Description:
Covered with winter wheat of about 4-5 cm in size.
The soil was hard, dry, and compact, with a thick clayey sediment cover. This part of the plot was recently ploughed to lose the soil.
More than half of the plant is dying.</td></tr>
<tr><td>Photographs</td><td>  </td></tr>
</table>

<table>
<tr><th colspan="2">Area 3</th></tr>
<tr><td>Information</td><td>Date: 14th March 2022
Coordinate: 46°48'53.28"N, 20°35'2.58"E
Trace of waterlogging: yes
Description:
Alfalfa is found at an average of 2 to 4 cm in size.
Waterlogging trace was not very clear due to newly ploughed and sowed land.
It also had a canal to drain excess water (see photographs).</td></tr>
<tr><td>Photographs</td><td>  </td></tr>
</table>

4. DATASETS

In this chapter, all the datasets used in this study, such as satellite data, agroclimatic data, and soil water content, are described. Moreover, this section also includes the crop development stages of winter wheat.

4.1. Satellite data

For this research, three different remote sensing products (S1, S2, and PS) were used for waterlogging detection and time series analysis to monitor crop development.

4.1.1. Sentinel-1

Sentinel-1 (C-band) Interferometric Wide (IW) swath at 5*20m spatial resolution offers both single and dual-polarization options- vertical transmission with vertical reception (VV) and vertical transmission with horizontal reception (VH) (ITC, 2019). Both polarizations (VV and VH) interact differently with water and land surface. The roughness of the surface can be detected with the VV polarization, which may be altered sometimes with the intervention of wind when observing the water surface. On the other hand, VH polarization performs better while detecting vegetation (Markert et al., 2020). For this study, only VV in descending orbit has been utilized for waterlogging detection, and both polarization in ascending and descending orbit has been used for time series analysis for crop development monitoring (Figure 8 and Table 2). This study uses the S1 (S1_GRD_FLOAT) dataset from Google Earth Engine (GEE) that is pre-processed using the Sentinel-1 Toolbox to remove thermal and border noise, perform radiometric calibration, and terrain correction. Additionally, median speckle filtering was applied (Figure 13). Radiometric terrain normalization were performed in GEE by the framework developed by Mullissa et al. (2021) to further remove the influence of topography on the SAR backscatter. Figure 8 shows the descending (left) and ascending (right) passes over the study area, and relative orbit 51, 175, 153, and 102 overlaps the Szarvas boundary. Therefore, S1 has frequent and consistent coverage over the study area. A total of 240 images (20 images/month) have been found for the time series analysis.

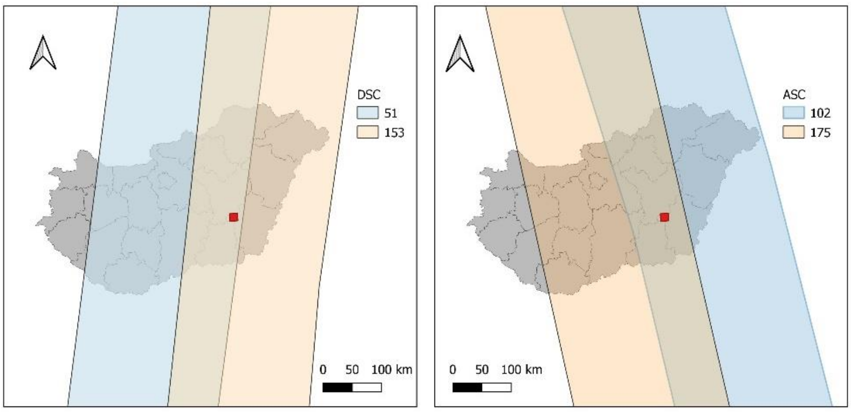

Figure 8: S1 descending (left) and ascending (right) passes in different relative orbital tracks covering the study area. The red box shows the study area in Hungary (gray shade).

Table 2: List of S1 GRD-IW data available over the study area.

Relative orbit	Pass	Local acquisition time
51	DESCENDING	04:54
175	ASCENDING	16:34
153	DESCENDING	04:46
102	ASCENDING	16:26

4.1.2. Sentinel-2

S2 consists of two multispectral satellites, namely 2A and 2B, offering five days of revisiting time together. S2 contains 13 spectral bands, including visible, near-infrared, and short-wave infrared. This study utilizes the freely available data from the "COPERNICUS/S2_SR" offered by GEE. This study area is covered by a total of 88 images (7 images/month) from two tiles which have been utilized for time series analysis (Figure 9, Figure 10, and Table 3).

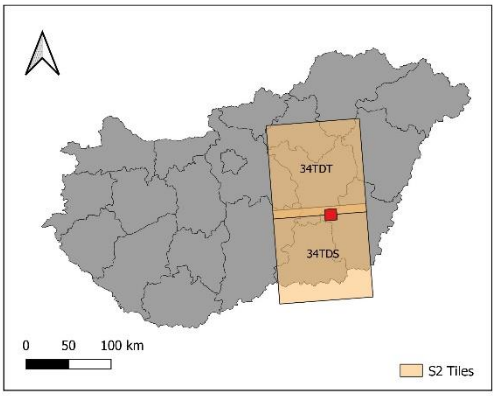

Figure 9: S2 tiles covering the study area. The red box indicates the study area in Hungary (gray shade).

Table 3: List of S2 data available over the study area.

Tiles	Pass	Local acquisition time
34TDT	DESCENDING	09:44
34TDS	DESCENDING	09:44

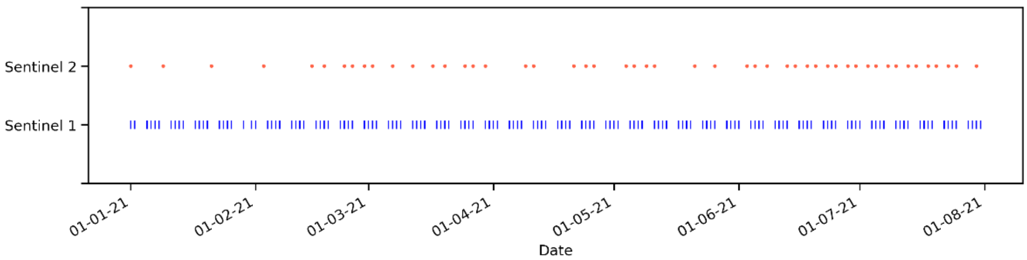

Figure 10: S1 and cloud-free S2 temporal coverage in the year 2021 over the study area. The collections include observations from all orbits.

4.1.3. PlanetScope

Planet's Dove Satellite provides daily observation of red, green, blue, and near-infrared bands at a ground sampling distance of 3.7–4.1 m, resampled to 3 m for final data products (Houborg & McCabe, 2016; Huang & Roy, 2021). This high-resolution spatial and temporal imagery creates new opportunities to monitor the agriculture field instantaneously, timely, and repeatably. PS constellation consists of 130+ satellites that enabled to achieve a revisit time of 1.5 days in 2020 globally over the land surface (Planet Labs, 2022; Roy et al., 2021). For this study, daily PS images were filtered from the Planet explorer (https://www.planet.com/explorer/) based on two search criteria- (a) 100% cloud-free of the area of interest and (b) acquisition period between November 2020 to March 2021 (potential waterlogging period). Fifteen cloud-free ortho tile images were found for further analysis. PS ortho tile images are ready-to-use data as the radiometric, sensor, and geometric corrections are performed on the images (Table 4). Therefore, no additional preprocessing step was applied to the selected images.

Table 4: PS surface reflectance ortho tile image description (Planet Labs, 2022).

Product Attribute	Description
Pixel size	3.125 m
Product Size	Tile size is 25km x 25km (8000 lines x 8000 columns)
Geometric Corrections	GCPs and high-resolution DEM (a post spacing of 30m to 90m) are used to orthorectify.
Atmospheric Corrections	Images are corrected with 6SV2.1 radiative transfer code, and additional correction has been done using near-real-time MODIS data (MOD09CMG and MOD09CMA).
Resampling method	Cubic Convolution

4.2. Agroclimatic data

This study uses NASA POWER reanalysis products for temperature and rainfall as there was no nearby ground weather station in the area studied. Results from Rodrigues & Braga (2021) proved that there is a good agreement between ground observations and the NASA POWER dataset. The agroclimatic data are available daily at 50km spatial resolution at the NASA POWER's website (https://power.larc.nasa.gov/).

4.3. Soil moisture

VanderSat (https://vandersat.com) utilizes Land Parameter Retrieval Model (LPRM) algorithm to retrieve 5cm depth of soil water content product at a spatial resolution of 100 x 100 m using their patent downscaling method (De Jeu et al., 2014; Owe et al., 2001; Owe et al., 2008). Thus, for this study, soil water content data provided by VanderSat retrieved from SMAP are used.

4.4. Crop growth stages

Crop growth stages and lengths for winter wheat are adapted from FAO (Allen et al., 2006), crop calendar (JRC-MARS, 2015), Biologische Bundesanstalt, Bundessortenamt und CHemische Industrie (BBCH) scale (Meier et al., 2018), and expert knowledge from the study area. The study period has been divided into growth stages to compare crop development in different crop growth stages. The growth stages for winter wheat are shown in Table 5. The date range for each growth stage does not represent the actual timing or duration of a particular stage in a given field; rather, it gives a probable time extent when a particular event (e.g., sowing/harvest) or process (e.g., senescence) takes place in the study area.

Table 5: Growth stages with the approximate length of winter wheat in Szarvas, Hungary.

Stages	Probable length (days)
Sowing	30
Initial (BBCH 0 to 9)	125
Leaf development (BBCH 10 to 30) and stem elongation (BBCH 30 to 39).	40
Flowering (BBCH 60 to 69) and fruit development (BBCH 70 to 79)	45
Senescence (BBCH 90 to 97)	15
Harvesting (BBCH 99)	30

5. RESEARCH METHODS

This chapter is divided into three sections. First, waterlogging detection methods are described. Second, time series analysis methods to monitor winter wheat development are discussed. Third, methods of mapping spatial patterns of NDVI deviation in NWL and WL locations are explained.

5.1. Waterlogging detection

In this section, methods of waterlogging detection with radar (S1) and optical (PS) images will be discussed.

5.1.1. Detection of waterlogging with PlanetScope Images

Waterlogging is highly dynamic over space and time due to rainfall events (and irrigation) (den Besten et al., 2021). Moreover, waterlogging usually appears in small patches in part of the agricultural plot, making it more difficult to detect with coarse resolution satellite images.

Optical observation cannot detect waterlogging under dense vegetation coverage due to the limitations of penetrating canopy (Lillesand et al., 2015). After investigating the winter wheat growth stages of the study area (Table 5), it is evident that the winter wheat plants are short in size during winter and pre-spring (November-March). Besides, this period receives very low temperature and high rainfall, which may trigger waterlogging. Thus, there are higher chances of capturing waterlogging during this period using remote sensing techniques. The processing steps of detecting waterlogging with PS images is illustrated in Figure 11.

NDWI takes advantage of the maximization of water reflectance on the green band and minimization of absorption of NIR by water (McFeeters, 1996). Therefore, NDWI has been selected as the desired index to separate WL spots using PS images.

$$NDWI = \frac{Green-NIR}{Green+NIR} \qquad \text{Equation 1}$$

The NDWI value ranges from -1 to +1, where McFeeters, (1996) used a thresholding of 0, indicating NDWI > 0 corresponds to water, and it is non-water if NDWI $\leq$ 0. However, the NDWI threshold value is not stable due to atmospheric interference and sun-target satellite geometry (Liu, 2012). Moreover, waterlogging in a part of an agricultural plot brings sediment from the other parts of the field. The sediments accumulated on the top surface of the WL locations, which makes it more complicated to separate the WL locations using NDWI. After calculating NDWI, all the images were inspected carefully for a threshold value. During the investigation, NDWI values were considered from the locations where traces of waterlogging were observed during fieldwork. Usually, the WL locations in the test sites exhibit NDWI values down to -0.27, while the value is more than zero for standing waterbodies such as the river and ponds. So, a threshold value of -0.27 was applied to separate water pixels where NDWI ≥ -0.27 are classified as water features.

After applying thresholding, the result is a bit image having water (= 1) and non-water pixel (=0). Then, all the bit images were summed up using the raster calculator, which resulted in a water frequency map. The NDWI values from buildings and building shadows were also classified as water. A building filtering has been done using the building layer (Annex C) to remove the misclassified water pixels in urban areas from the waterlogging map.

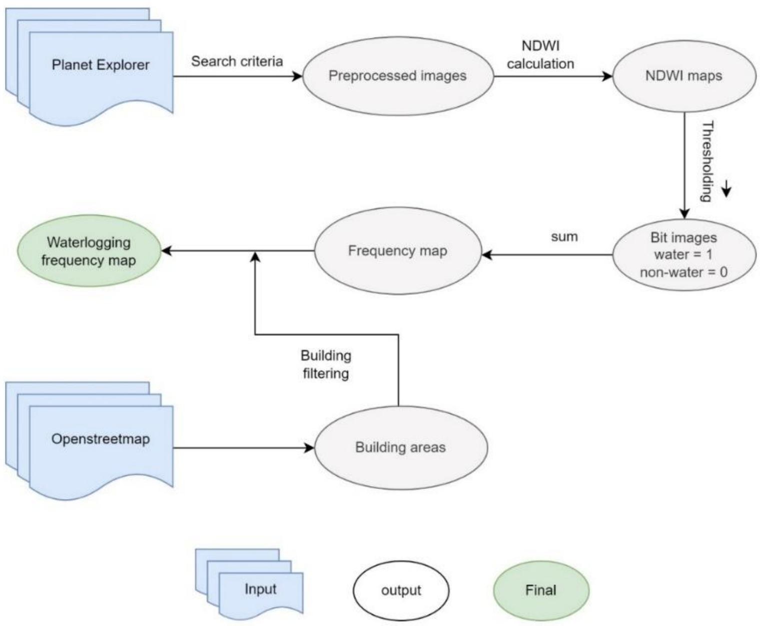

Figure 11: PS waterlogging mapping process.

5.1.2. Detection of waterlogging with radar Images

The processing steps for detecting waterlogging with S1 images are illustrated in Figure 12. Waterlogging detection with radar is possible when the WL surface acts as a medium of specular reflection where radar signals are reflected away from the sensor, causing low backscatter. The surface of the other features is usually rougher than the water surface, which triggers diffuse reflection and results in higher backscatter values (Ovakoglou et al., 2021). However, waterlogging detection with radar becomes tough when signals from other pixels interfere with the original backscatter of the pixels, especially in a small area consisting of few pixels. The distinct characteristics of the backscatter mechanism of water compared to other features allow to separate WL locations by applying a threshold. The global thresholding method (e.g., Otsu thresholding) is not an effective technique for detecting a very low amount of water as the image histogram will not exhibit bimodality due to the strong influence of other features. For better accuracy in capturing waterlogging with radar, visual inspection and knowledge of the area are crucial in selecting an appropriate threshold value. In this study, pixels are classified as WL if the pixel values are less than the selected threshold, whereas pixels larger than the threshold are considered NWL pixels. In GEE, a total of 44 S1 images were found during the winter and pre-spring season (between October 2020 to March 2021). S1 images are already pre-processed for essential correction in the GEE platform (Gorelick et al., 2017).

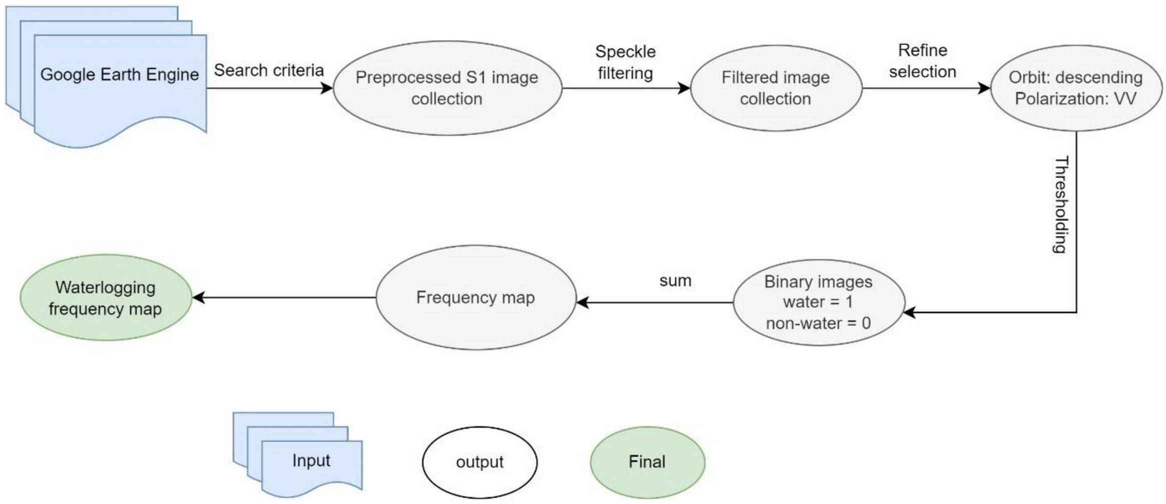

Figure 12: S1 waterlogging mapping process.

Several speckle filtering options were explored, and the median filter was selected as it was able to detect small waterlogged places (Figure 13). As the waterlogging detection will be done through the thresholding method, images were taken from the same orbits (descending) and polarization (VV) to avoid misclassification of WL locations. Values of S1 σ_{VV}^{0} were inspected from some pre-selected WL locations where waterlogging traces were found during the fieldwork. After several 'trial and error,' a threshold value of -16 dB has been applied over the whole image collection. Thus, all the pixels from the image collection with values less than -16 dB correspond to WL locations. Finally, the waterlogging map has been generated by adding all the WL pixels from all the binary images.

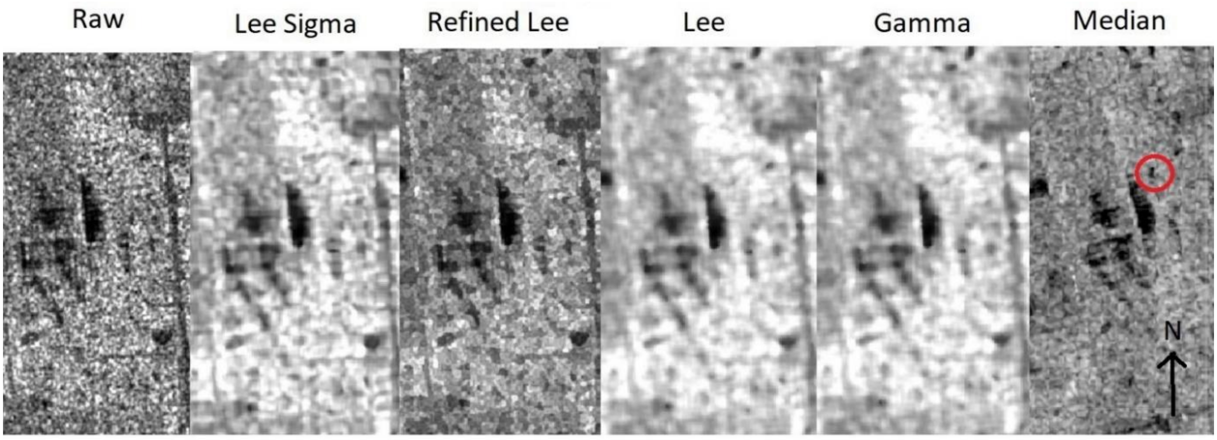

Figure 13: Evaluation of different speckle filtering methods to detect waterlogging. The red circle in median filtering indicates a small WL place which is cleared out in other filtering options.

5.1.3. Sensitivity analysis of the threshold selection

Figure 14A, B show the results of sensitivity analysis in selecting threshold values for separating WL areas from PS and S1 images. A threshold of NDWI ≥ -0.27 on PS images was applied, and results of -0.27 ±0.02 are also presented in Figure 14A. To separate the waterlogged areas from S1 images, a threshold of $\sigma_{VV}^{0} \leq$ -16 dB was employed. Results of the -16 dB ± 1dB are depicted in Figure 14B.

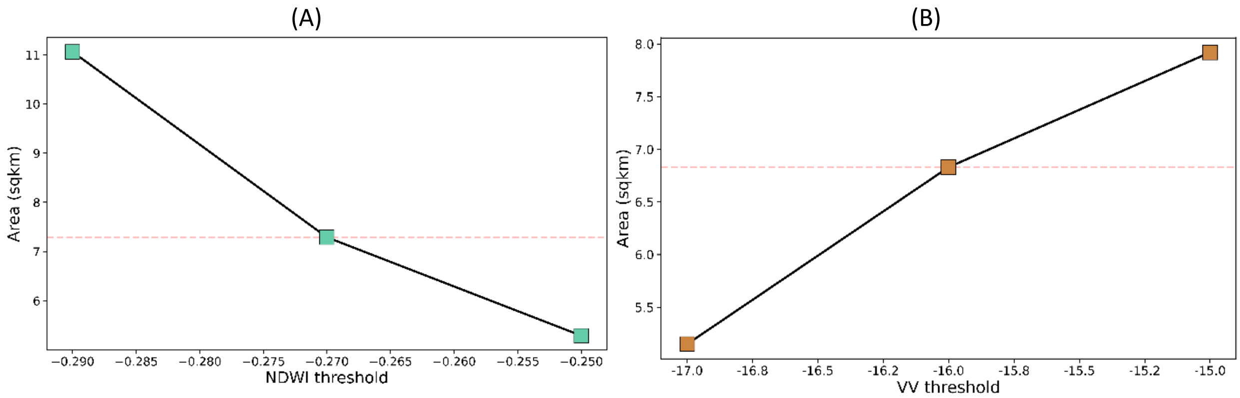

Figure 14: Sensitivity analysis of different NDWI and VV backscatter threshold values over PS and S1 images, respectively, in detecting waterlogging. The red dash lines indicate the selected threshold and corresponding WL areas for the study.

5.2. Combination of optical and radar waterlogging map

All the binary images from PS having water (= 1) and non-water pixel (=0) are resampled to 10m. Then, a combined PS and S1 waterlogging extent and observed frequency map was produced by adding all the binary images from PS and S1. Places with waterlogged pixels from both maps are counted double if the pixels belong to different dates while counted once if present on the same date.

5.3. Time series analysis

Remote sensing time series can be used for a wide range of applications, such as detecting flooded vegetation (Tsyganskaya, 2019), monitoring crops (Khabbazan et al., 2019), and deriving phenology (Meroni et al., 2021). Time series analysis has been utilized in this study to assess the temporal dynamics of vegetation response. Values from NDVI, CR, RVI (calculated from Table 6), and backscatter coefficient values were extracted for two types of masks.

Table 6: Equations used for calculating NDVI, CR, and RVI.

Equations	Comments
NDVI = $\frac{NIR-RED}{NIR+RED}$ (2)	Here, NDVI is the Normalized Difference Vegetation Index, RED is the visible red band, and NIR is the Near-Infra-Red band.
$CR = \frac{\sigma_{VH}^{0}}{\sigma_{VV}^{0}}$ (3)	Here, σ_{VH}^{0} and σ_{VV}^{0} are dual-polarized backscatter coefficients. The RVI equation for S1 is adapted from (Nasirzadehdizaji et al., 2019).
$RVI = \frac{4\sigma_{VH}^{0}}{\sigma_{VV}^{0} + \sigma_{VH}^{0}},$ (4)	

For crop monitoring, field-level and intra-field level mean values were extracted for all the wheat parcels, and intra-field level masks were delineated for WL and NWL locations from the waterlogging map. To avoid false-positive results, intra-field level WL masks were created when there is water in both optical and radar-based waterlogging maps. The time series of the mean of NDVI, CR, RVI, and backscatter coefficients were generated from all the 22 wheat parcels, including 7 test areas where waterlogging occurred. The standard deviation was used to show the homogeneity and heterogeneity of the vegetation response at a single point in time.

$$stdev = \sqrt{\frac{1}{n} * \sum_{i=1}^{n} x_i^2 - x_{avg}^2} \quad \text{..} \textit{equation 5}$$

Here, $stdev$ is the standard deviation from all the masks, n is the number of pixels in the mask, x_i is the value of i^{th} pixel, extracted from the images and x_{avg} is the average of the values extracted from the mask.

Satellite data can be noisy and contaminated from the disturbance caused by clouds, atmosphere, and even faulty sensors, which remain after pre-processing the raw data. For this study, the rolling mean and Savitzky–Golay filter (Savitzky & Golay, 1964) have been explored to smoothen the time series for better interpretation. The rolling mean misses the first eight observations, and the phase of the time series delays in both NDVI and CR when applying the rolling mean by taking a window size of 9. A window size of 9 and first-order polynomial degree have been considered in Savitzky–Golay filtering. Savitzky–Golay filter shows excellent results in smoothing out the noise from the signals by retaining the original pattern of the observations (Figure 15).

Figure 15: Smoothening of CR from S1 using rolling mean (green line) and Savitzky–Golay (gray line).

5.3.1. Time series analysis of Normalized Differential Vegetation Index (NDVI)

NDVI uses red (absorbed by vegetation) and near-infrared (reflected by vegetation) channels to quantify vegetation health (equation 2). Time series of NDVI are useful to monitor the change in vegetation response due to changes in local climate (Zhang et al., 2003). NDVI can be used as a proxy for photosynthesis activity as it can sense chlorophyll activity (Boori et al., 2019). Thus, the NDVI time series gives an idea of crop health throughout different growing stages. NDVI value ranges from -1 to 1, where the higher value indicates healthier vegetation. NDVI change is noticeable in different phenological stages (Wardlow & Egbert, 2010); specially peak and drop of NDVI values during the growing period and harvest, respectively (Lenney et al., 1996). NDVI in WL crops showed lower values than NWL plants, according to the research of den Besten et al. (2021) in a sugarcane plantation area located in Mozambique. The NDVI equation (equation 2) is applied to S2 image collection in GEE.

5.3.2. Time series analysis of the backscatter coefficient

Time series of backscatter coefficients were generated at the field and intra-field level for 2021. The mean of the pixels over a selected area reduces the speckle effect from the observations. However, an additional smoothing filter was applied to reduce the sharp peaks and drops from the time series (Figure 15). The time series of backscatter values are compared with rainfall and soil moisture to explain sudden drops and peaks in the observations.

5.3.3. Time series analysis of CR and RVI

Volume scattering increases with vegetation, and cross-polarization reveals volume scattering. As a result, the thicker the vegetation cover is, the higher the cross-polarization value (Vreugdenhil et al., 2018). Moreover, a strong correlation exists between CR from SAR and optical vegetation indices (e.g., LAI and biomass) (Ferrazzoli et al. 1992; Mc Nairn et al. 2014). In agricultural remote sensing, RVI is also used as an alternative for NDVI in optical observation to monitor vegetation growth (Kumar et al., 2013). So, in this study, CR (equation 3) and RVI (equation 4) will be compared with NDVI to see how crop development changes throughout the season in optical and radar vegetation responses.

5.3.4. Time series of combined S1 and S2

CR is an indicator of vegetation canopy volume because of volume scattering and vegetation water content (VWC) (Veloso et al., 2017a), whereas NDVI shows chlorophyll activity of the vegetation (Rouse et al., 1974). In this study, an effort was made to combine optical and radar vegetation response by taking the proportion of scaled CR from S1 and NDVI from S2 to evaluate differences in crop development in WL and NWL crops throughout the growing stages.

5.4. Mapping spatial patterns of NDVI deviation in NWL and WL locations

NDVI in WL fields shows less homogeneity than in NWL fields (den Besten et al., 2021). So, NDVI at the intra-field level can be used to show the spatial pattern of the NDVI deviation between NWL and WL locations. For this study, three S2 images were selected from three major growth stages- 1. leaf development and stem elongation (9th April 2021), 2. flowering and fruit development (21^{st} May 2021), and 3. senescence (23^{rd} June 2021). Then NDVI was calculated for each image using equation 2. After that, NWL pixels are delineated using the combined S1 and PS waterlogging map (explained in 6.2.4). Mean NDVI for NWL pixels in each field was calculated. Then the deviation is calculated by simply subtracting the NDVI value of each pixel from the mean NDVI calculated from NWL pixels (Figure 16). This returns a value in each pixel where a higher positive value indicates a hampered crop development, and a lower positive to high negative value implies healthy vegetation conditions.

$$NDVI_{dev} = \overline{NDVI}_{nwl} - NDVI_i \text{...} \quad \text{equation 6}$$

Here, $NDVI_{dev}$ is the NDVI deviation in i_{th} pixel, $\overline{NDVI}_{nwl}$ is the mean NDVI from NWL pixel and $NDVI_i$ is the NDVI in i_{th} pixel.

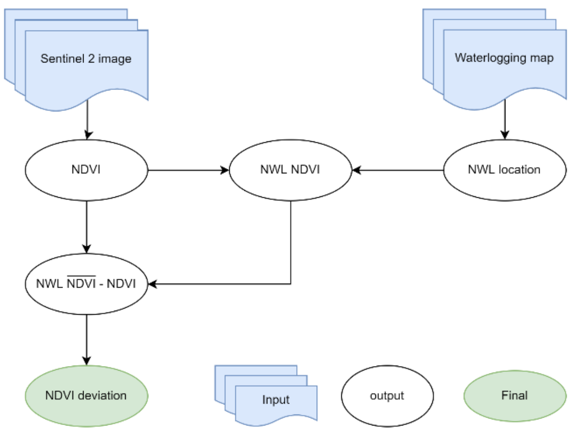

Figure 16: NDVI deviation mapping process.

6. RESULTS AND DISCUSSION

This section describes the results of agroclimatic factors, mapping waterlogging dynamics, time series analysis, and crop development monitoring, variability of satellite data in WL and NWL fields, and mapping spatial patterns of NDVI deviation in NWL and WL locations.

6.1. Agroclimatic factors

Daily precipitation, soil water content (SWC), and daily mean temperature data are illustrated in Figure 17. From October 2020 to December 2021, total precipitation was 580 mm in the study area. Frequent rainfall events were observed till March 2021, with a high number of rainy days, especially in January and February 2021. However, the amount of precipitation in this period did not exceed 10 mm on most days. PS cloud-free images show the study area was under snow cover between January 18 to 25 and February 12 to 17.

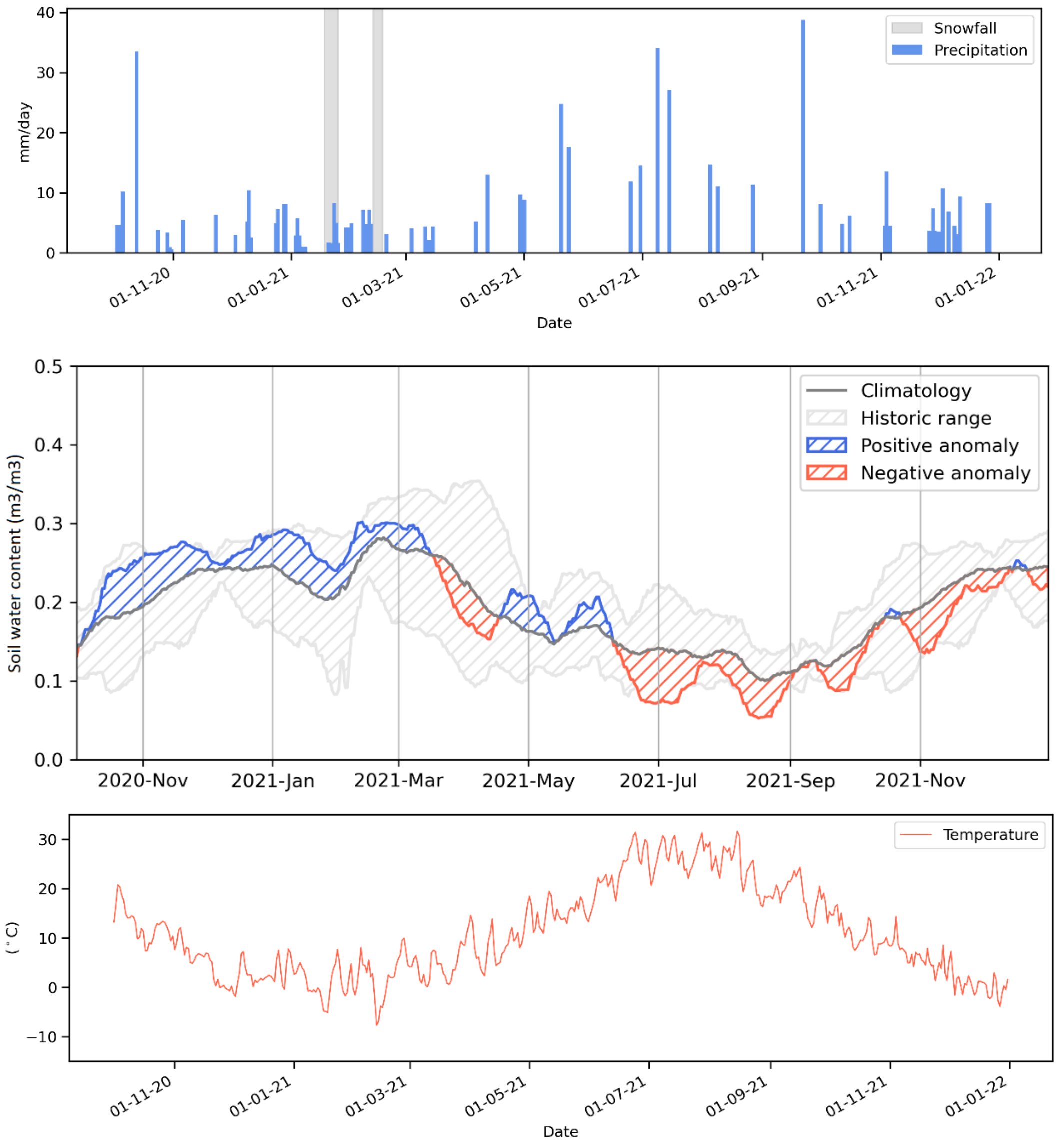

Figure 17: Precipitation [mm d^{-1}] (top), SWC [m^3m^{-3}] (middle) and temperature [℃] (bottom) data in Szarvas, Hungary. The gray shaded bars in the top plot show the snow cover days over the area, and the blue bars are the rainfall events. The gray line in the middle plot refers to climatology (average SWC of 5 years), and the gray color fill is the historical range of SWC. Positive and negative anomaly indicate the higher and lower observed SWC than climatology. The red line in the bottom plot depicts the daily mean temperature.

The soil moisture plot (middle) shows a wet period between October 2020 and mid-March 2021. The possible reason behind the drop in the observation in December and January is the snow cover and freezing soil over the study area. The wettest period with SWC of about 0.3 m^3m^{-3} is observed in the month of February 2021. The lowest drop in the temperature is found in January and February 2021 at -5 °C and reaches the highest peak at around 30 °C in July and August.

6.2. Mapping waterlogging dynamics

Mapping waterlogging dynamics requires the identification of waterlogging extent, occurrence, and timing. This research uses optical (PS) and radar (S1) images to detect and map waterlogging extent and occurrence spatially. A detailed method of identification and mapping of waterlogging has been discussed in section 5.1.

6.2.1. PlanetScope waterlogging map

Figure 18 shows the distribution of observed waterlogging extent and occurrence based on the PlaneScope images from November 2020 to March 2021. Permanent water bodies are depicted in blue and separable from the WL places. The gradient red color palette displays the waterlogging extent where deep red pixels correspond to places where water is detected frequently (multiple times), and light red shows a low occurrence of waterlogging, as recorded by the PS images. The Körös river runs on the north-western side. The river's floodplain became flooded during the observation period. The total area of observation is 181.42 km^2 where 2.36% of it is found as permanent water bodies (Table 7). About 7.17 km^2 (3.95%) of the area has been observed as WL from the PS images.

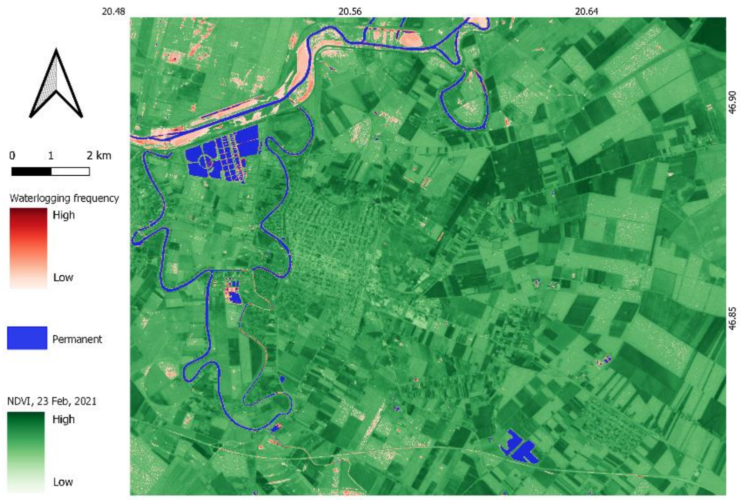

Figure 18: Spatial distribution waterlogging extent and occurrence detected from PS images in Szarvas, Hungary. The blue color indicates permanent water bodies, and the red color ramp shows observed water frequency. PS NDVI in green gradient color ramp is used as a background.

6.2.2. Sentinel-1 waterlogging map

Waterlogging extent and occurrence have been mapped in the period of November 2020 to March 2021 using S1 images. The final waterlogging map from radar images is shown in (Figure 19). Similar to the PS waterlogging map, rivers and ponds are illustrated in blue and WL places are in red gradient shade. The waterlogging map from S1 shows some WL places distributed in the southwestern part of Szarvas. From the S1 observations, 6.83 km^2 (3.76%) of the area was directly affected by the waterlogging.

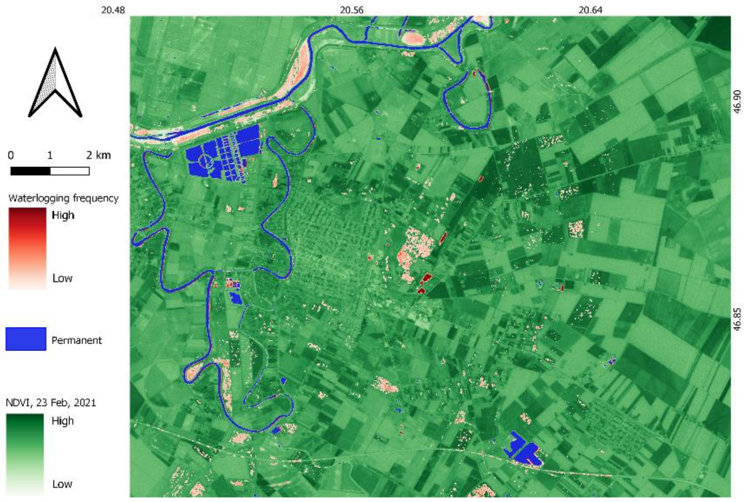

Figure 19: Spatial distribution waterlogging extent and occurrence detected from S1 images in Szarvas, Hungary. The blue color indicates permanent water bodies, and the red color ramp shows observed water frequency. PS NDVI is used as a background.

Table 7: Statistics of waterlogging area.

	PS (km^2)	Percentage	S1 (km^2)	Percentage
NWL	174.25	96.04	174.59	96.23
WL	7.17	3.95	6.83	3.76

	Area (km^2)	Percentage
Permanent waterbodies	4.26 km2	2.36

6.2.3. Comparison of optical and radar in waterlogging detection

The detection of waterlogging from optical images is based on surface reflectance and absorption capability of the NIR band by the water, whereas radar detects waterlogging when the backscatter is reflected away. So the pixels appear dark on the images (McFeeters, 1996; Ovakoglou et al., 2021). Figure 20 compares waterlogging maps of selected agricultural fields, defined using PS and S1 data in Szarvas, Hungary. In Figure 20 (a1, a2, c1, and c2), waterlogging detection with S1 is underestimated compared to PlaneScope observation. There can be two reasons why waterlogging detected by PS is different from S1 detection. Firstly, PS offers high spatial resolution (3m), which enables water separation even in small places (Mishra et al., 2020), where having a lower resolution (10m), S1 could not be able to separate the small WL places. Secondly, water detection with S1 is problematic if, within a pixel, the surface is rough and mosaiced with patches of sediments in shallow WL locations. Moreover, noise from nearby pixels in S1 makes it difficult to delineate WL places when water appears in patches. Therefore, in Figure 20 (c1), PS successfully detected narrow stripes of water, whereas, in Figure 20 (c2), water pixels are not visible in S1 observations.

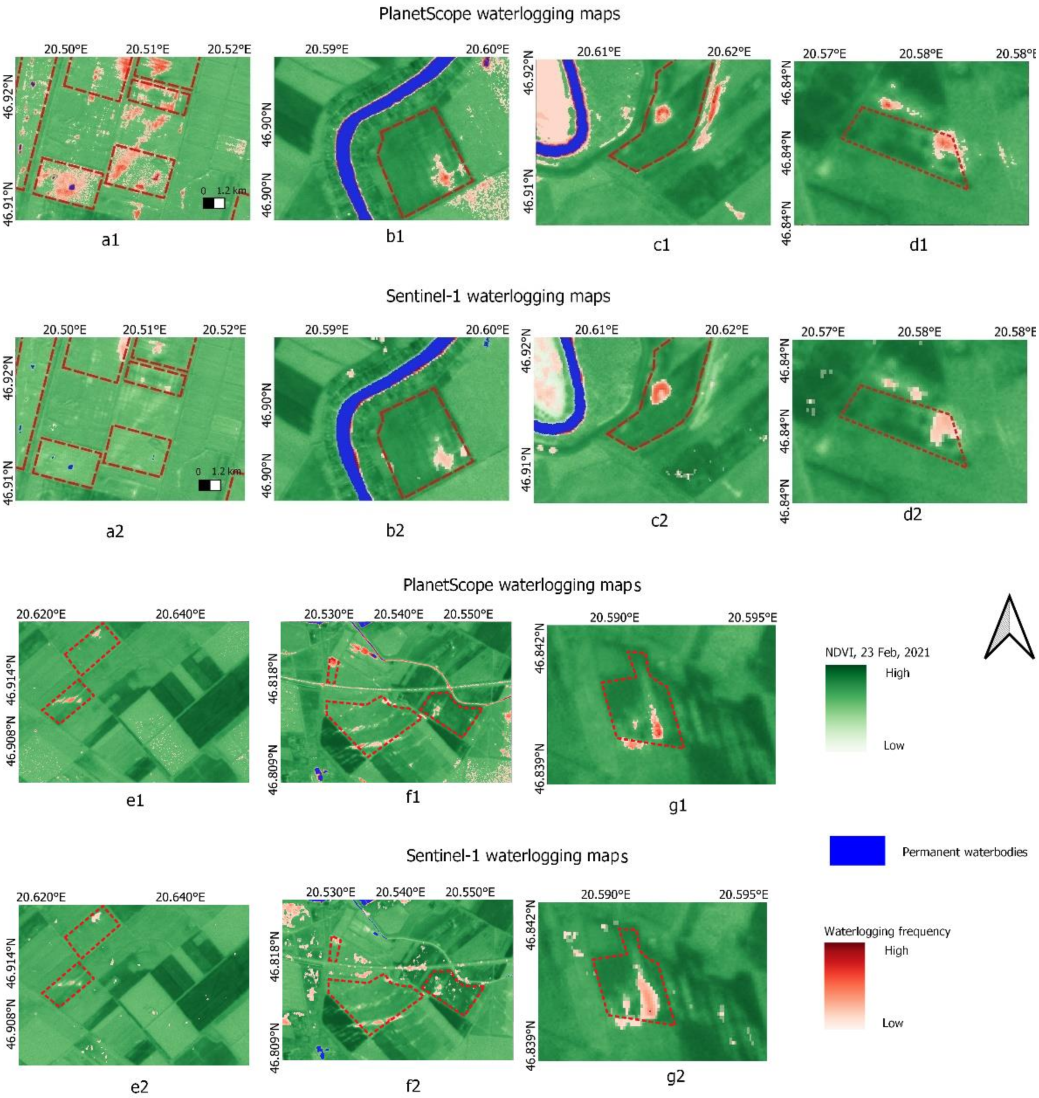

Figure 20: Comparison of the waterlogging maps from S1 and PS.
The blue color indicates permanent water bodies, and the red color ramp shows observed water frequency. The fields are delineated with a red dashed line, and PS NDVI is used as a background.

6.2.4. Combined optical-radar waterlogging map

Figure 18 and Figure 19 indicate that PS and S1 have capabilities in detecting waterlogging. However, cloud cover restricts high-resolution PS from observing over WL locations where moderate resolution S1 SAR sensors have no interference in observing waterlogging during cloudy days. Therefore, PS has high spatial detection capability with fewer observations, and on the other hand, S1 offers regular observations with high temporal waterlogging detection capability. Figure 21 shows the waterlogging extent and occurrence map derived from combined PS and S1 data, which can be considered as a better representation of waterlogging in terms of spatial and temporal detection.

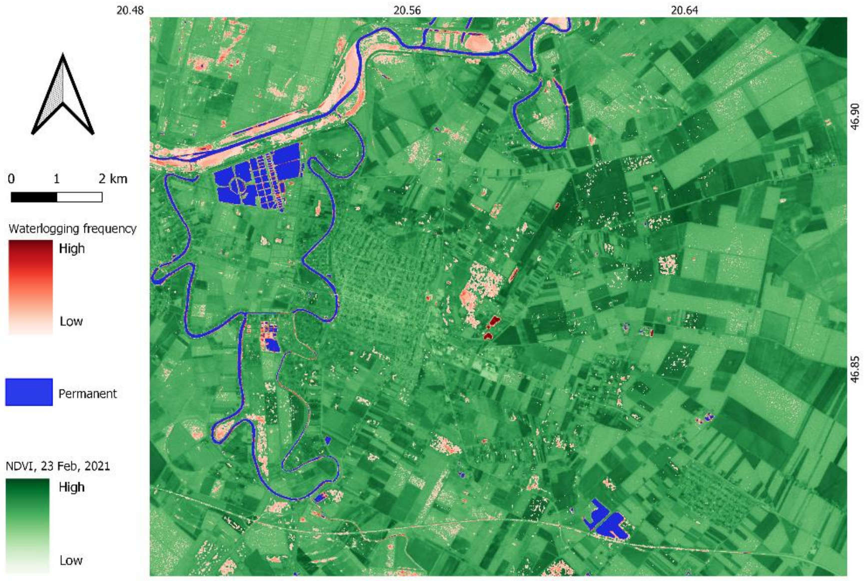

Figure 21: Waterlogging extent and observed water frequency detected from combined S1 and PS observations in Szarvas, Hungary.
The blue color indicates permanent water bodies, and the red color ramp shows observed water frequency. PS NDVI is used as a background.

6.2.5. Waterlogging timing

The scatterplots of mean σ^0_{VV} and σ^0_{VH} in WL and NWL locations reveal the waterlogging moments (Figure 22). Between January, February, and March in 2021 show high discrepancies in S1 backscatter between WL and NWL locations, whereas, in other months, the relationship is positive and stronger. Discrepancies between WL and NWL locations between January and March are evidence of the presence of waterlogging. After harvest at the end of June, backscatter from bare soil in WL and NWL locations are showing a strong relationship. If the discrepancies are due to roughness differences, then the backscatter from WL and NWL locations would show inconsistency again after the crop being harvested.

Figure 23 shows the probable waterlogging timing based on the time series of S1 σ^0_{VV} (dB). Time series from different WL locations show that σ^0_{VV} (dB) in WL locations have comparatively lower values than in NWL locations. When the locations were in NWL state, σ^0_{VV} (dB) values ranged from -8 to – 10 dB. A gradual drop in σ^0_{VV} (dB) indicates waterlogging and where the drops are sharp (about 5 to 10 dB) in WL locations compared to NWL locations. The drops in WL locations are observed from 8th December 2020 in Area 6 and 14, where from 20 to 25 January 2021 in Area 2, 16, 26, 27, and 29. The steady drops (about 2 to 5 dB) in NWL are observed due to the growth of winter wheat plants between March and April. From Figure 17, it is evident that rainfall was frequent, and soil moisture was higher than the historical average from October 2020 to March 2021.

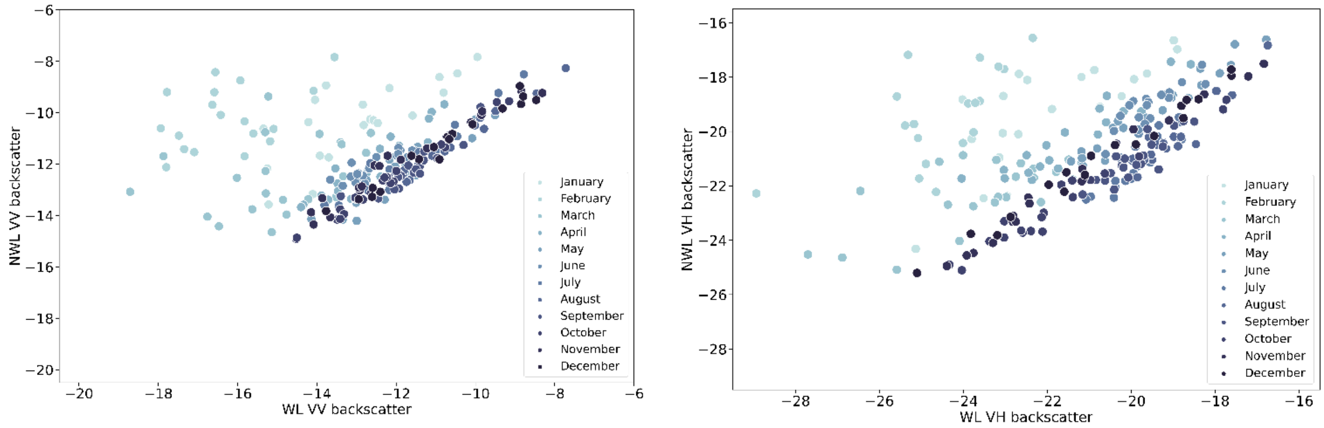

Figure 22: Scatterplot of mean VV backscatter (left) and VH backscatter (right) between WL and NWL areas.

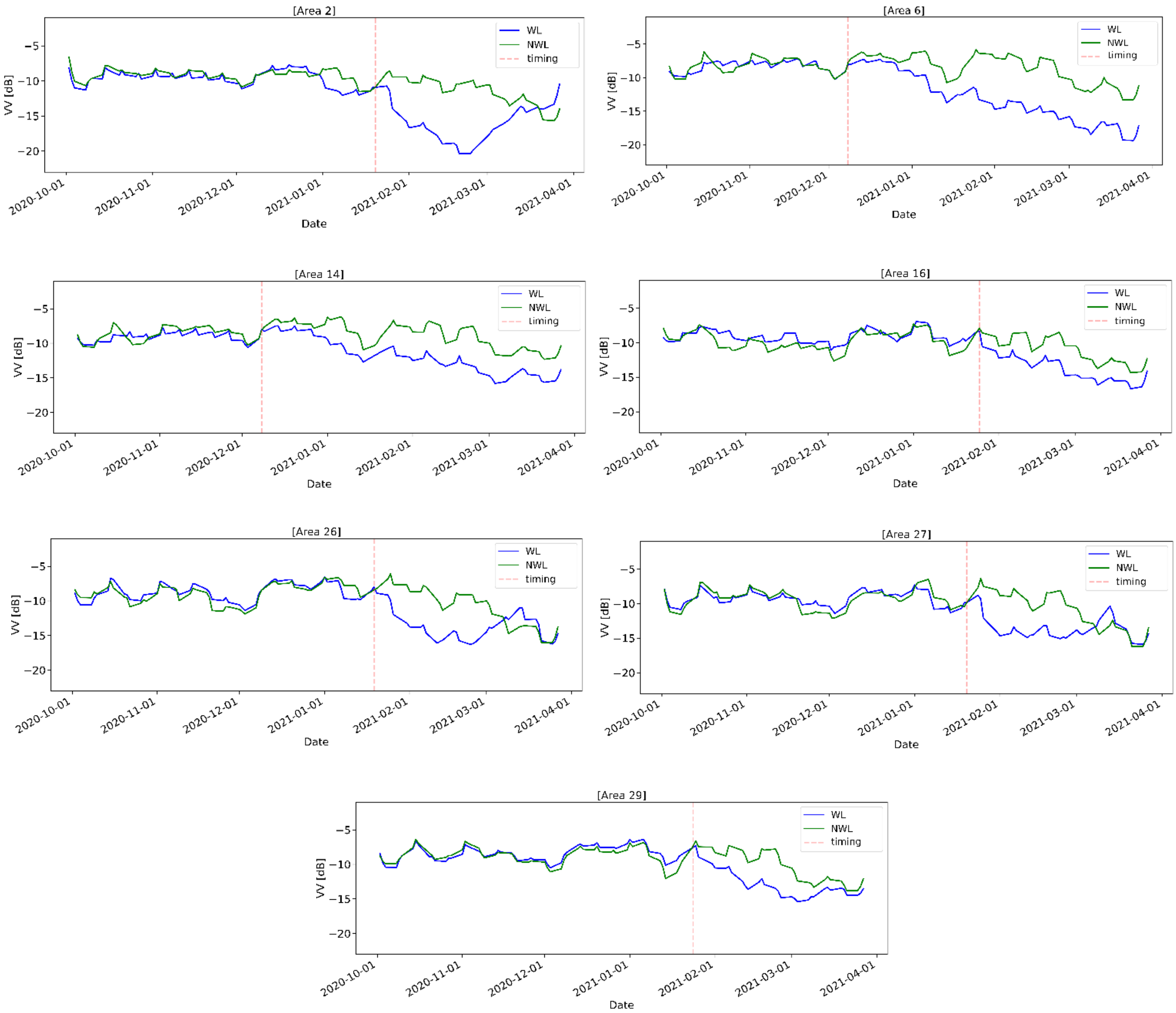

Figure 23: Time series of S1 VV backscatter (dB) in WL (blue) and NWL (green) areas within the same parcels. The red dash lines are probable waterlogging timing breakpoints created based on visual inspection when inconsistency starts between WL and NWL locations.

6.3. Time series analysis and crop development monitoring

6.3.1. Temporal profile of S2 NDVI in wheat fields

NDVI is an indicator of the leaf area and chlorophyll activity, which change over the growing stages of crops (Rouse et al., 1974). Field-level average S2 NDVI was calculated to understand the crop development of winter wheat throughout different growing stages (Figure 24). Winter wheat is sowed around October-November (Table 5), and after emergence, the plant stays in dormancy for the entire winter season in Hungary. The mean NDVI during this stage is less than 0.4 in January and February, as the canopy cover of winter wheat is very little at this stage. From March, the mean NDVI rises progressively during the leaf development and stem elongation stage (BBCH 10-39) and reaches 0.6 at the end of April due to increased canopy cover. The highest mean NDVI value of 0.7 is found during the flowering and fruit development stage (BBCH 60-79) at the beginning of June. At the end of June, the mean NDVI starts to decrease due to the loss of chlorophyll during the senescence period. The sharp decline of mean NDVI (to 0.2) is due to the harvest at the beginning of July. The standard deviation is very low after the harvesting period from July to October as all the fields are stubbles.

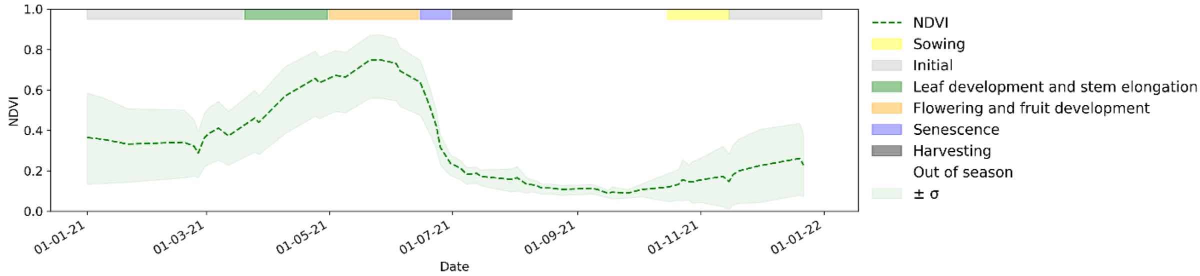

Figure 24: Temporal profile of S2 NDVI for all wheat parcels (n=22) in Szarvas, Hungary.
As reported in the legend, the green dash line and the green shaded areas indicate the mean and ± one standard deviation. Time series from each wheat parcel are extracted by taking the average of all pixels located in the field boundary. The colored bar on the top of the chart indicates the growth stages from Table 5.

6.3.2. Temporal profiles of S1 backscatter coefficient in wheat fields

The temporal profile of the mean S1 backscatter coefficients for 22 wheat parcels is shown in Figure 25 for different growth stages. During the winter, short vegetation remains undetectable with radar, and the variation in the backscatter coefficient is attributed to the change in soil moisture and surface roughness (Veloso et al., 2017b). At the beginning of January 2021, the values of σ^0_{VH} and σ^0_{VV} are -16 dB and - 7 dB, respectively. There are two sharp decreases of about 7-8 dB in both σ^0_{VH} and σ^0_{VV} backscatter in January and 4-5 dB in February. These abrupt drops are caused by frozen soil (Khaldoune et al., 2011) and snow cover (Figure 17). Moreover, a snow-covered surface introduces low radar signals because of specular reflection and absorption loss in water (Scherer et al., 2005).

The sharp decline (5 dB) at the end of January can be related to waterlogging from snowmelt as standing water appears as a smooth surface which introduces specular reflection and results in lower backscatter (section 2.1.1). Moreover, frequent rainfall events are recorded during this time of the year (Figure 17). In April, winter wheat biomass starts to accumulate, and as a result, σ^0_{VH} and σ^0_{VV} increase gradually by about 5 dB. During leaf development and stem elongation period, there is a 5 dB steady rise of σ^0_{VH} due to volume scattering (Wiseman et al., 2014) and the double bounce effect between wheat stalk and surface (Brown et al., 2003; Picard et al., 2003). The σ^0_{VV} backscatter, which is influenced by surface and canopy, remained lower (at -14 dB) in this stage due to attenuation by the vertical structure of the wheat stems (Brown et al., 2003). From May to mid-June, an increase about 3-4 dB is noticeable in both σ^0_{VH} and σ^0_{VV} as winter wheat goes through flowering, fruit development, and ripening stages. This increase is due to the opening of flag leaves, inflorescences, flowering, fruit development, and ripening (Khabbazan et al., 2019).

There is an abrupt decrease in VV, and VH backscatter at the end of June is due to winter wheat harvesting.

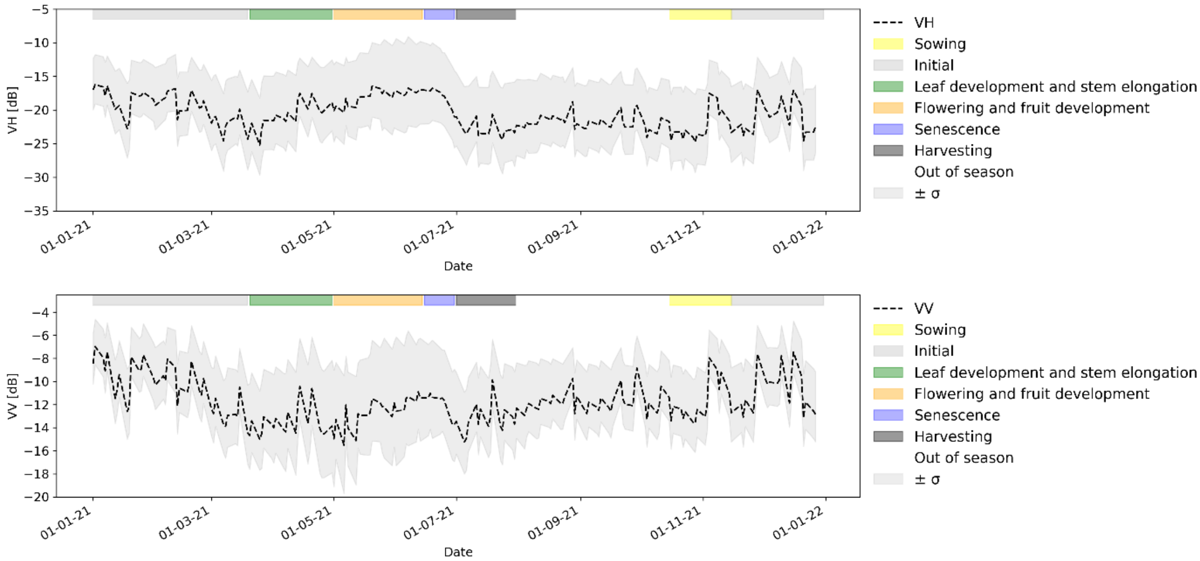

Figure 25: Temporal profile of S1 backscatter data for all wheat parcels (n=22) in Szarvas, Hungary; (top) VH backscatter (dB) and (bottom) VV backscatter (dB).
As reported in the legend, the black dash line and grey shaded areas indicate the mean and ± one standard deviation. Time series from each wheat parcel are extracted by taking the average of all pixels located in the field boundary. The colored bar on the top of the chart indicates the growth stages from Table 5.

6.3.3. Temporal profile of S1 CR and RVI in wheat fields

S1 CR is a stable crop growth indicator as it reduces the double-bounce effect and errors caused by sensors and environmental factors (Brown et al., 2003). Similarly, RVI is not much sensitive to environmental conditions but more sensitive to biomass and VWC (Kumar et al., 2013). As Figure 26 demonstrates, both mean CR (dB) and mean RVI show similar temporal patterns for winter wheat. CR and RVI remained stable in January and February at 9-10 dB and 4-5, respectively. A significant increase of about 3-4 dB in CR and 0.5 in RVI is observed between April and May. This rise can be attributed to the increase of fresh biomass and volume scattering in leaf development and stem elongation stage (BBCH 11-39).

The mean NDVI value started to increase in March, earlier than the CR and RVI. This can be explained by the significant contribution of ground in radar backscatter when the plant is short in size, where increasing NDVI is due to the greenness of the sparse vegetation. CR and RVI are relatively constant at 5 dB and 1.0, respectively, from May to mid-June due to the stabilization of above-ground biomass in the flowering stage (BBCH 60-69). Between June 20 and 1st July, CR, and RVI decreased slightly due to the loss of VWC during the senescence period (BBCH 90-97). At the beginning of July, there was a steep decline of CR to -11 dB and RVI to 0.4 due to harvesting.

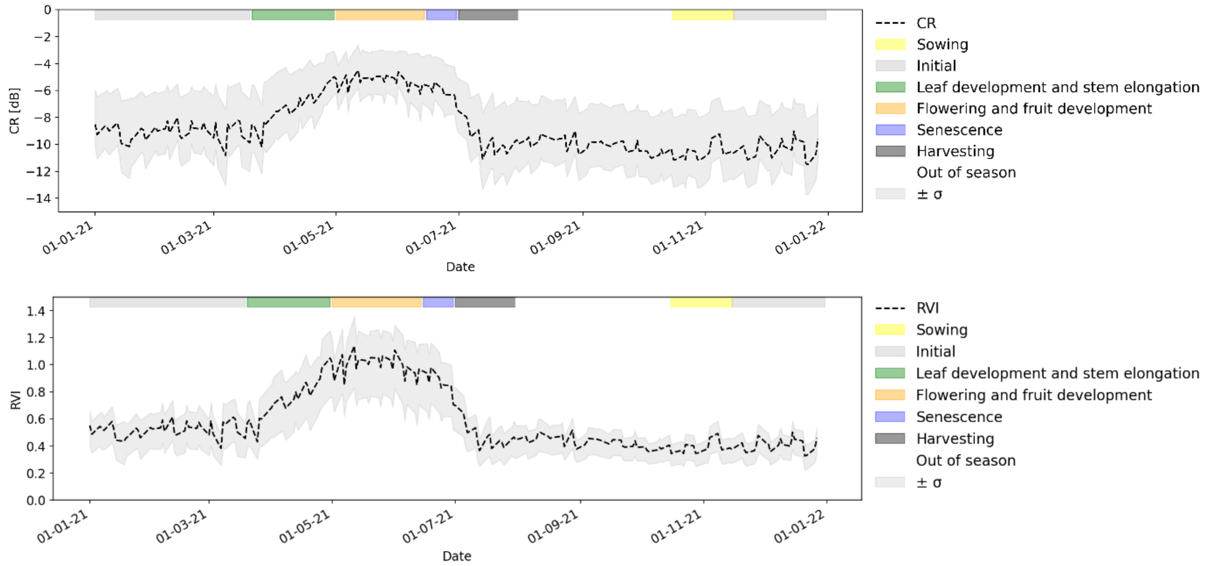

Figure 26: Temporal profile of S1 (top) CR (dB) and (bottom) RVI for all wheat parcels (n=22) in Szarvas, Hungary. As reported in the legend, the black dash line and grey shaded areas indicate the mean and ± one standard deviation. Time series from each wheat parcel are extracted by taking the average of all pixels located in the field boundary. The colored bar on the top of the chart indicates the growth stages from Table 5.

6.4. Variability of satellite data in WL and NWL fields

6.4.1. Time series analysis of backscatter coefficient in WL and NWL locations

There is practically no or very sparse vegetation cover during winter as wheat plants go through a long dormancy period. So, the backscatter received from the VH and VV mostly comes from soil roughness and SWC. Figure 27A, B depicts a progressive decrease (8 to 10 dB in NWL) from January to April in VH and VV backscatter, which can be explained by the lower backscatter from smooth soil over the surface due to the accumulation of fine sediments transported by rainfall events or snow melts. During February, there is an abrupt drop in σ_{VH}^0 and σ_{VV}^0 in WL spots due to waterlogging, causing specular reflection of σ_{VV}^0 and σ_{VH}^0. The decline in σ_{VH}^0 is about 4 to 5 dB, and for σ_{VV}^0, the drop is about 7-8 dB. It can be explained by the sensitivity of σ_{VV}^0 in detecting surface roughness better than σ_{VH}^0 (Markert et al., 2020). Between April to May, the number and size of the leaf and stem increase, indicating the accumulation of VWC in winter wheat plants (Veloso et al., 2017b). Figure 27A shows a rise in σ_{VH}^0 due to double-bounce and volume scattering in leaves and stems between April and May, as explained in Lopez-Sanchez et al. (2013) and Wiseman et al. (2014). The VV backscatter increases due to high VWC from the leaf as the VV backscatter is dominated by canopy and soil surface (Brown et al., 2003). The σ_{VV}^0 and σ_{VH}^0 for the WL location show slightly (1 to 2 dB) less values than the NWL location in Area 26 and 27.

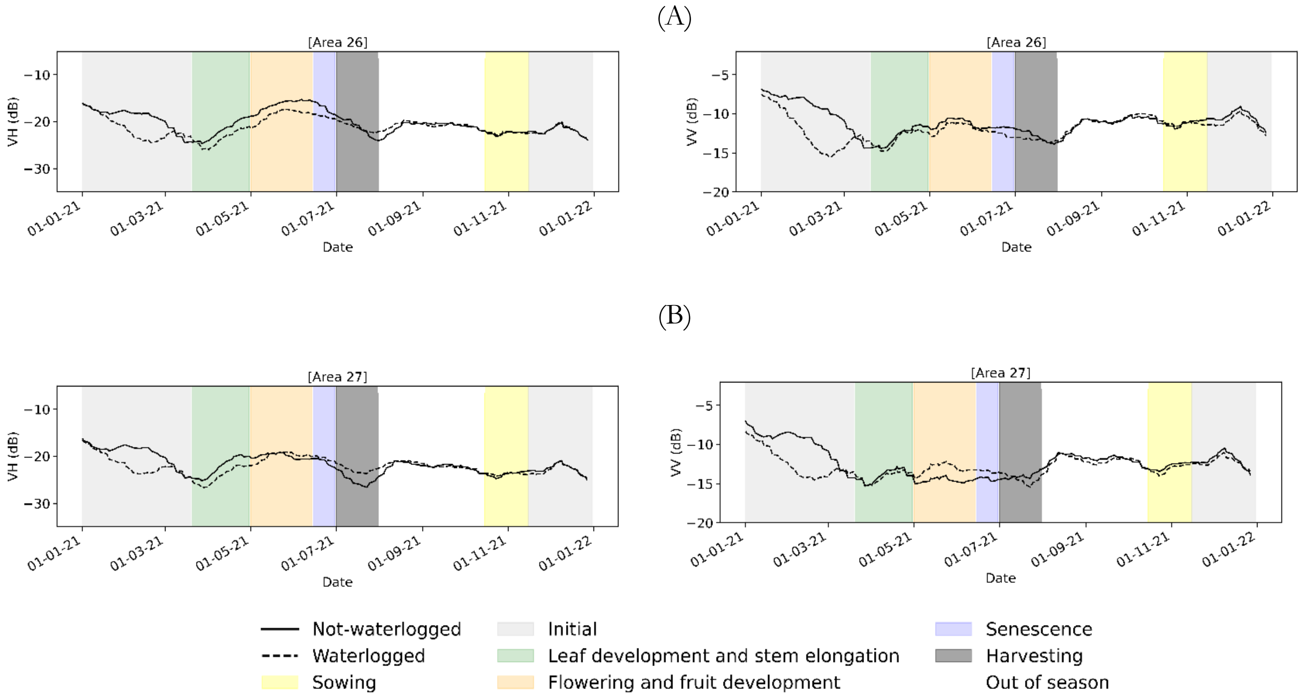

Figure 27: Time series of S1 VH backscatter and VV backscatter in WL and NWL locations in wheat fields in Szarvas, Hungary. Time series for all locations are extracted by taking the average pixels located in the part of the field (WL and NWL). As reported in the legend, the colored bar in the background indicates the growth stages from Table 5.

On the other hand, σ_{VV}^{0} in the WL location is less than in the NWL location, where a negligible difference is found in σ_{VV}^{0} in April. In contrast, there is no difference between WL and NWL locations, where a decrease in NWL locations is found in May. In Area 26, slightly lower values in σ_{VV}^{0} and σ_{VH}^{0} are found in WL spots, whereas in Area 27, NWL shows a slightly lower value (1 dB) in σ_{VV}^{0}, and there is no difference in σ_{VH}^{0} for WL and NWL wheat during the senescence stage. The time series of S1 backscatter for other WL and NWL locations are provided in Annex A.

6.4.2. Time series analysis of NDVI, CR, and RVI in WL and NWL locations

Figure 28 presents NDVI and CR in WL and NWL locations for seven wheat fields. NDVI values are 0.3 to 0.4 for Area 2, 14, and 16 at NWL locations and 0.1 to 0.2 at WL locations from January to March when wheat plants have low canopy cover. On the other hand, the NDVI value is less than 0.2 for NWL and WL locations in Area 6, 26, 27, and 29. All seven area experienced a gradual drop to less than 0.1 in NDVI for WL locations starting from January till March. This drop can attribute to the waterlogging condition as the NDVI value is close to zero values in the case of water and bare soil surfaces (Carlson et al., 1994). NDVI starts to increase during the leaf development and stem elongation stage (BBCH 10-39) and reaches about 0.6 in NWL locations at the end of April, and a difference of 0.1-0.2 (Area 2, 16, 26, 27, and 29) and 0.3 -0.4 (Area 6 and 14) is noticeable between WL and NWL locations. The highest values (0.7- 0.8) of NDVI is observed during the flowering and fruit development stage (BBCH 60 to 79) from May to mid-June. The highest values of NDVI in WL are delayed compared to the NWL locations for about 10-12 days (Area 14, 16, and 27). The impact is highest in Area 6 and 14 with an NDVI difference of 0.3 to 0.4 and lowest in Area 2 with a difference of less than 0.1 in this growth stage. During the senescence stage (BBCH 90- 97), NDVI declines together in both NWL and WL locations. This is due to the termination of chlorophyll activity when winter wheat loses greenness (Veloso et al., 2017a). NDVI in all areas drops suddenly to 0.2 at the end of June due to harvesting.

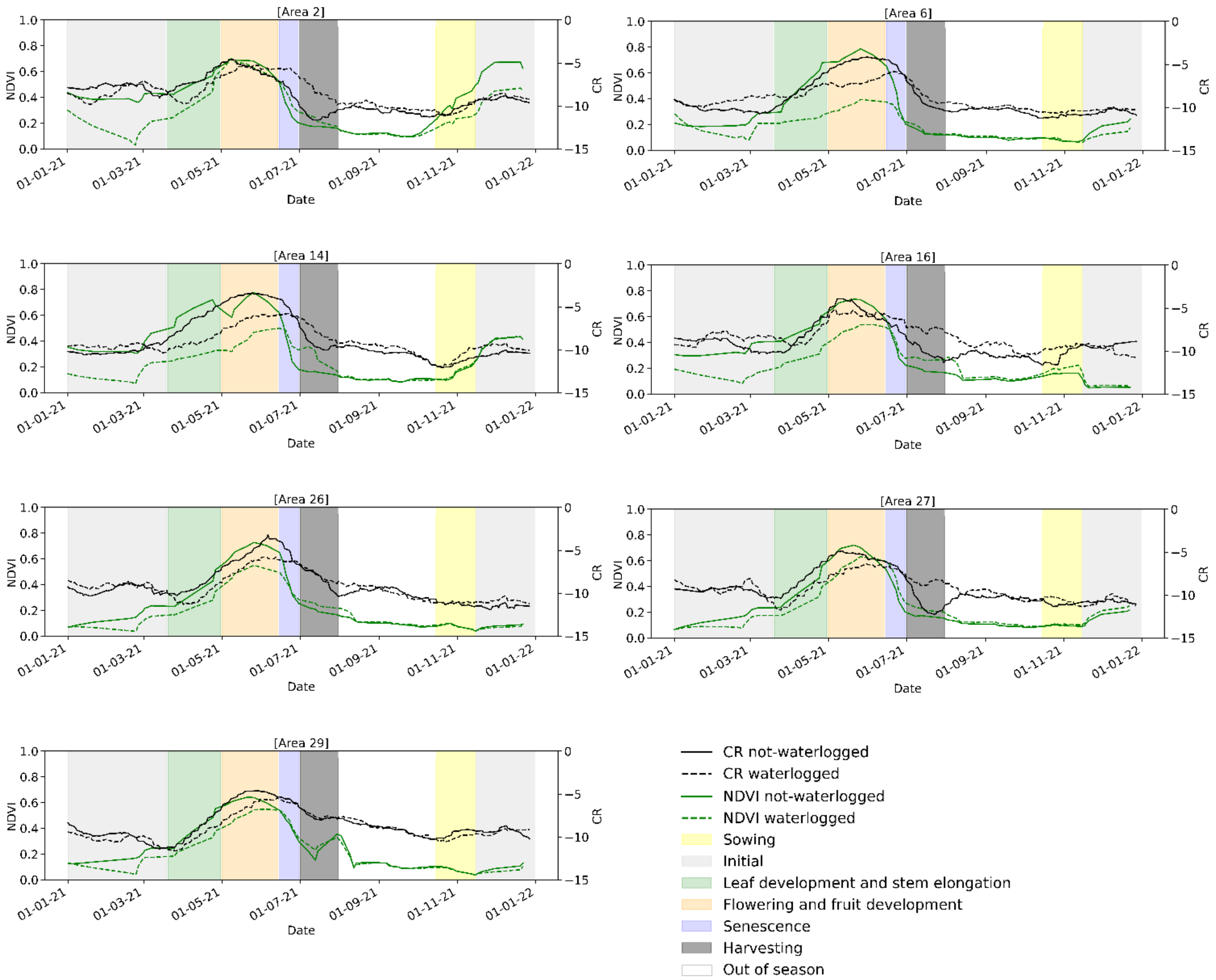

Figure 28: Time series of S1 CR and S2 NDVI in WL and NWL locations in different wheat fields in Szarvas, Hungary. Time series for each area is extracted by taking the average of pixels located in the part of the field (WL and NWL). As reported in the legend, the colored bar in the background indicates the growth stages from Table 5

Figure 28 reveals that CR stays stable at 8-10 dB during the initial period when wheat plants are too short to detect by radar observations. The significant contribution to backscatter mostly comes from surface roughness and soil moisture in this stage. CR increases during the leaf development and stem elongation stage (BBCH 10-39) in April, when the biomass accumulates. In this stage, CR values in WL locations are about 3 dB less than NWL locations in Area 2 and 14, whereas less than 2 dB lower values are observed in other WL locations. The highest values of CR are found in May and June when flowering and fruit development (BBCH 60 to 79) occurs. There is a noticeable difference in CR values (about 3-4 dB) at WL and NWL locations (the latter show higher values) at Area 6 and 14 during this stage. At Area 16, 26, 27, and 27, CR values show a 2 dB difference between the WL and NWL locations. CR starts to drop as the VWC decreases during the senescence (BBCH 90-97) and declines sharply when harvested (BBCH 99). After harvesting, CR in WL locations exhibits higher values (maximum 3 dB) than CR in NWL locations. This rise in WL locations can be explained by the growth of weeds or grass attracted by wet soil.

Despite having different scales in RVI and CR, the time series pattern is identical in monitoring winter wheat in different growth stages (section 6.3.3). In Figure 29, RVI follows a similar trend as CR (Figure 28) in detecting WL and NWL winter wheat crop changes throughout different growth stages. However, it is noticeable that the RVI difference is higher than in CR between NWL and WL locations in May when winter wheat shows the highest values and goes through the flowering and fruit development stage (BBCH 60 to 79). This reveals that RVI is demonstrating better results in illustrating the impact of waterlogging on crop development.

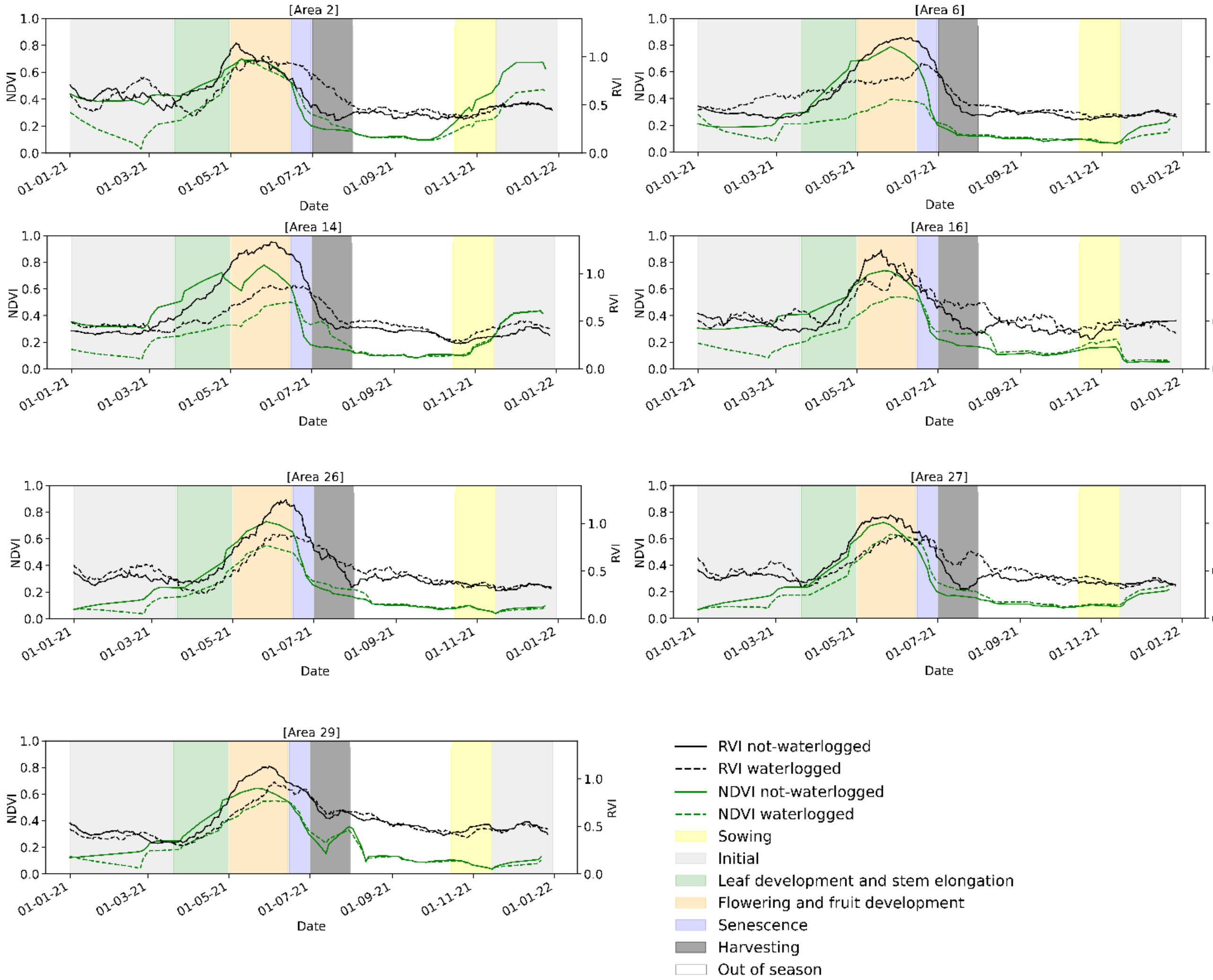

Figure 29: Time series of S1 RVI and S2 NDVI in WL and NWL locations in different wheat fields in Szarvas, Hungary. Time series for each area is extracted by taking the average of the pixels located in the part of the field (WL and NWL). As reported in the legend, the colored bar in the background indicates the growth stages from Table 5.

Optical (NDVI) and radar vegetation indicators (CR or RVI) show distinct characteristics when monitoring crop (winter wheat) in NWL and WL locations. In Area 6, 14, and 16, the NDVI difference in NWL and WL locations is much more significant (well separable) than CR or RVI in April (Figure 28 and Figure 29). From May to mid-June, the differences in NDVI and CR or RVI for NWL and WL imply the recovery of winter wheat from waterlogging stress. However, in other locations, the impact of waterlogging on winter wheat is much clearer when NDVI and CR or RVI hits the maximum point during the flowering and fruit development stage. The effect of waterlogging cannot be detectable with NDVI during the senescence as winter wheat in both NWL and WL locations reduce greenness (chlorophyll), and NDVI starts to drop simultaneously.

6.4.3. Agreement between different satellite data in WL and NWL locations

Correlation analysis between Mean CR, NDVI, σ^0_{VH}, σ^0_{VV}, and RVI from all the WL (orange) and NWL (green) locations has been done to observe their relationship in WL and NWL states. The results are visualized in the form of histograms and scatterplots in Figure 30, and correlation coefficients are displayed in Figure 31. The histograms in the diagonal part of Figure 30 are the distribution of the satellite data. Figure 31 shows that the highest correlation (r = 0.98) occurs between CR and RVI in both NWL and WL locations, as CR and RVI are derived from S1 and are sensitive to roughness and VWC. The correlation between CR and NDVI is 0.86 in NWL locations and 0.78 in WL locations. On the other hand, the correlations between NDVI and RVI in NWL and WL locations are 0.87 and 0.83, respectively. So, RVI is more comparable to NDVI and better representative of plant growth monitoring in both NWL and WL crops (winter wheat). Besides, the correlation between σ^0_{VH} and CR decreases from r = 0.75 in NWL locations to r = 0.61 in WL locations because of discrepancies in σ^0_{VH} and σ^0_{VV} during the waterlogging. In contrast, the correlation between σ^0_{VH} and σ^0_{VV} is stronger in WL locations (r = 0.6), whereas weaker agreement (r = 0.44) is found in NWL locations. This can be explained by the similar response of σ^0_{VH} and σ^0_{VV} to waterlogging during the initial stage.

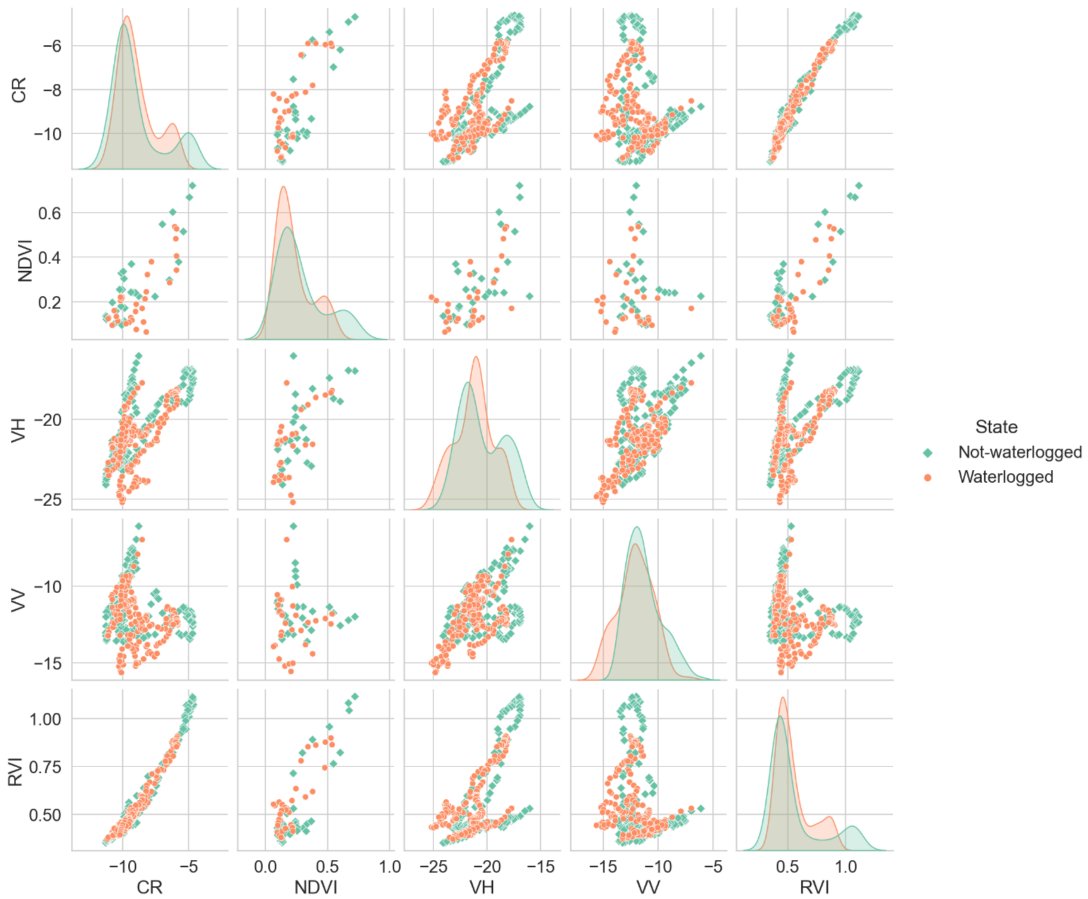

Figure 30: Correlogram between mean CR, NDVI, RVI, VH and VV backscatter where the color indicates the state of waterlogging. The green color is NWL, and the orange color is WL locations.

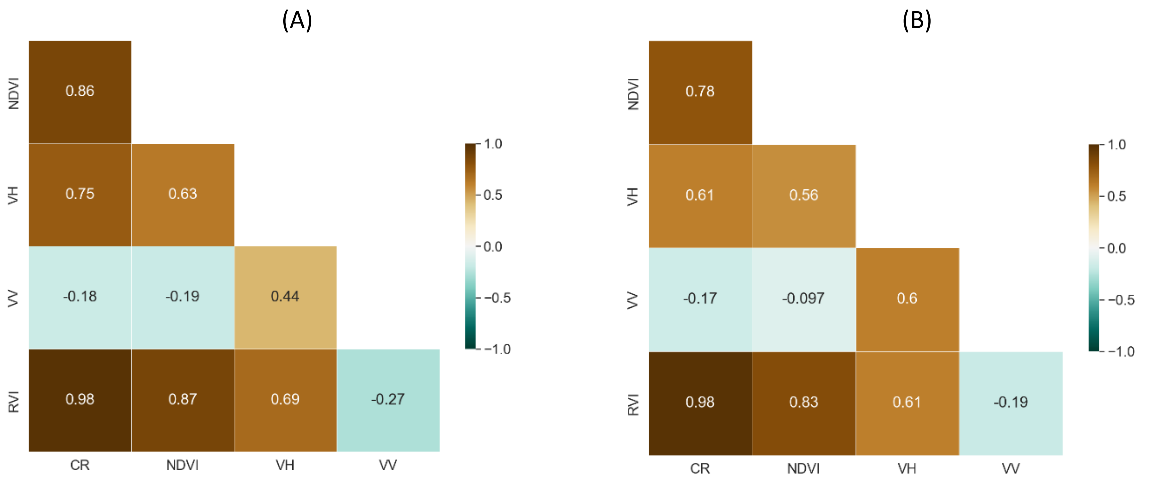

Figure 31: Pearson correlation coefficients between mean CR, NDVI, VH, and VV backscatter in (A) NWL and (B) WL locations.

6.4.4. Distribution of CR and NDVI of WL and NWL locations in different crop growth stages

Figure 32 compares how CR from S1 and NDVI from S2 is distributed over different crop growth stages in NWL and WL locations. During the initial stage, NDVI values between the lower and upper quartile in NWL locations (Figure 32: A) are distributed from 0.2 to 0.4, whereas for WL locations (Figure 32: B), NDVI values are found between 0 to 0.2. This happens because of sparse short canopy cover in WL locations compared to NWL locations because of waterlogging impact. During the leaf development and stem elongation stage, winter wheat starts to grow, and NDVI from NWL locations are uniformly distributed in lower (0.2) and upper (0.6) quartiles, whereas for WL locations, NDVI values are concentrated between 0.2 to 0.4. This reveals the waterlogging stress on winter wheat resulting in lower NDVI in WL locations. Maximum NDVI peak is found during the flowering and fruit development stage. During the flowering and fruit development stage, the highest NDVI is found between 0.6 to 0.8 and 0.45 to 0.65 in most NWL locations and WL locations, respectively. During the senescence, NDVI drops very sharply when winter wheat loses chlorophyll. This is why the NDVI from NWL locations are sparsely distributed in a larger range (0.8 to 0.1). However, NDVI values from WL locations are distributed in a higher range (0.7 to 0.2) compared to the NDVI values from NWL locations. This difference can be explained by the delayed winter wheat growth in WL locations.

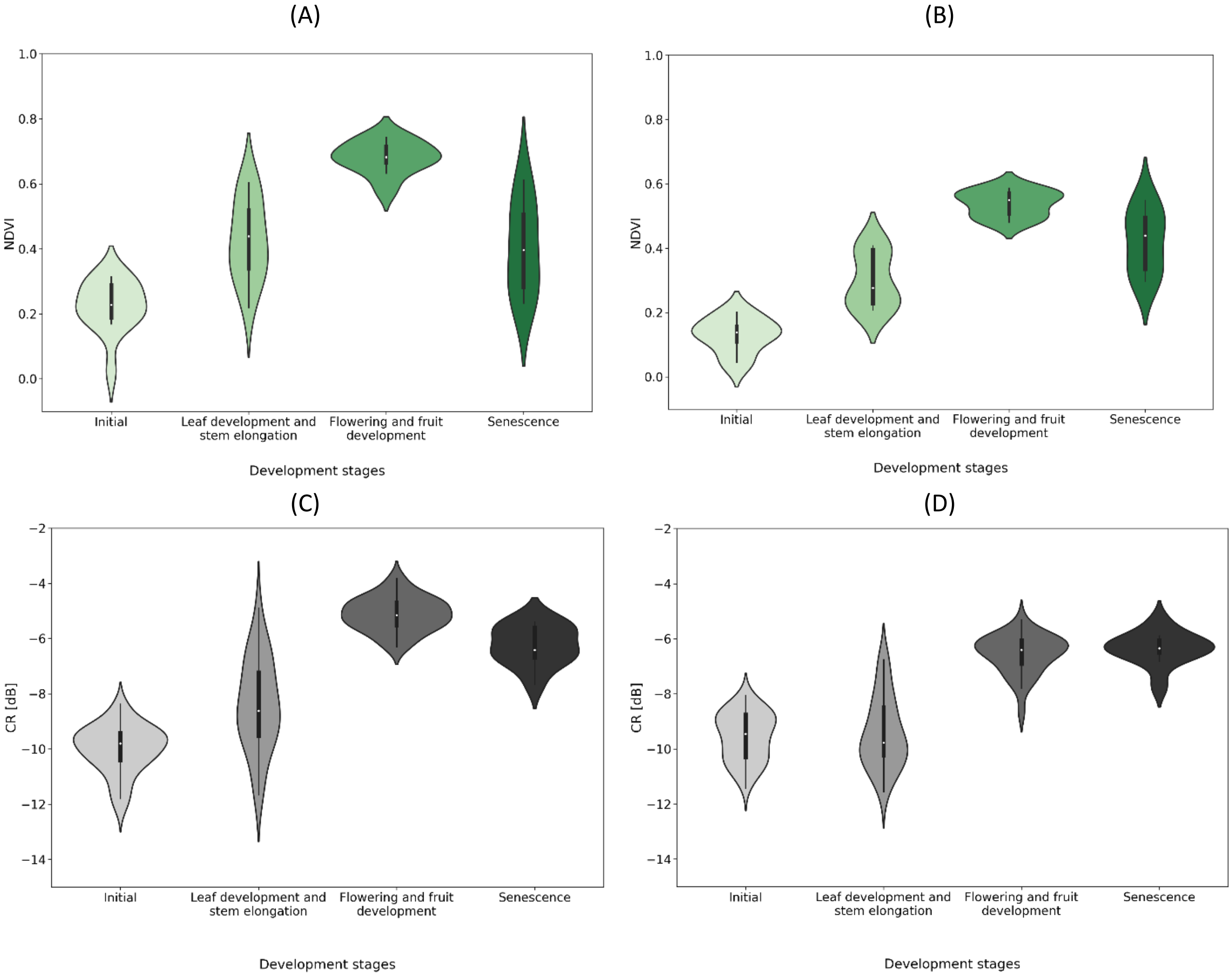

Figure 32: Violin plot of the distribution of mean satellite responses in different crop growth stages in NWL and WL locations over the growing season of 2021.
(A) NDVI in NWL, (B) NDVI in WL, (C) CR in NWL, and (D) CR in WL locations.

Figure 32 C, D show the CR is very much concentrated in – 10 dB in NWL locations where CR values from WL locations are primarily distributed within the -9 to -11 dB range during the initial stage when waterlogging explains the increased CR values in some WL locations. During the leaf development and stem elongation period, CR has a value range distributed between -4 to -12 dB (upper to lower quartile) for NWL locations and -6 to -12 (upper to lower quartile) for WL locations. The median of CR values in WL locations are declined (to -10 dB) in this stage compared to the initial stage because significant backscatter contribution is coming from the canopy, wherein in the initial stage, high soil moisture from bare soil is the responsible for the increased CR in WL locations. During the flowering and fruit development stage, CR values are distributed in -4 to -6 dB (upper to lower quartile) in NWL locations and -6 to -8 dB (upper to lower quartile) in WL locations. This is due to the limited growth of winter wheat, which resulted in a waterlogging-induced lower value range (2 dB difference) for CR in WL locations. During the senescence stage, a lower CR value range (-5 to – 7.5 dB) compared to the previous growth stage reveals the loss of VWC in NWL locations, whereas a slightly higher CR range (-5 to-7 dB) is noticeable in WL locations. This can be explained by the delayed winter wheat crop growth in WL locations due to the impact of waterlogging.

6.4.5. Combined NDVI and CR (scaled) time series in NWL and WL locations

Figure 33 shows the combined response of NDVI and CR in NWL and WL locations in crop growth stages. In Area 2, 6, and 16, the values for NWL and WL locations are about 1, which indicates the same values of NDVI and CR in January. On the other hand, there is a higher discrepancy between WL and NWL locations as CR shows higher values in January for Area 14, 26, and 27. Between February and March, values for NWL locations range from 1 to 5, and the range is 3 to 14 for WL locations. This is due to the sensitivity of radar signals (increased CR) to waterlogging during the initial stage when there is no or short canopy. During the leaf development and stem elongation stage (April), good agreement between NWL and WL locations is observed as the canopy cover increases. Similar values are also found during the flowering and fruit development stage from May to mid-June when canopy cover and growth is the maximum. This confirms that CR and NDVI have similar capabilities for detecting crop development in the WL and NWL conditions when the major contribution in reflectance and backscatter comes from the canopy (and stems). During the senescence stage, values gradually increase in both NWL and WL locations simultaneously as winter wheat plants lose VWC and chlorophyll. Lastly, NWL locations have lower values than WL locations (Area 2, 6, 16, and 27) and higher WL locations (Area 26 and 29) after harvesting due to NDVI and CR variation originating from weed and grass coupled with high soil moisture found in WL locations.

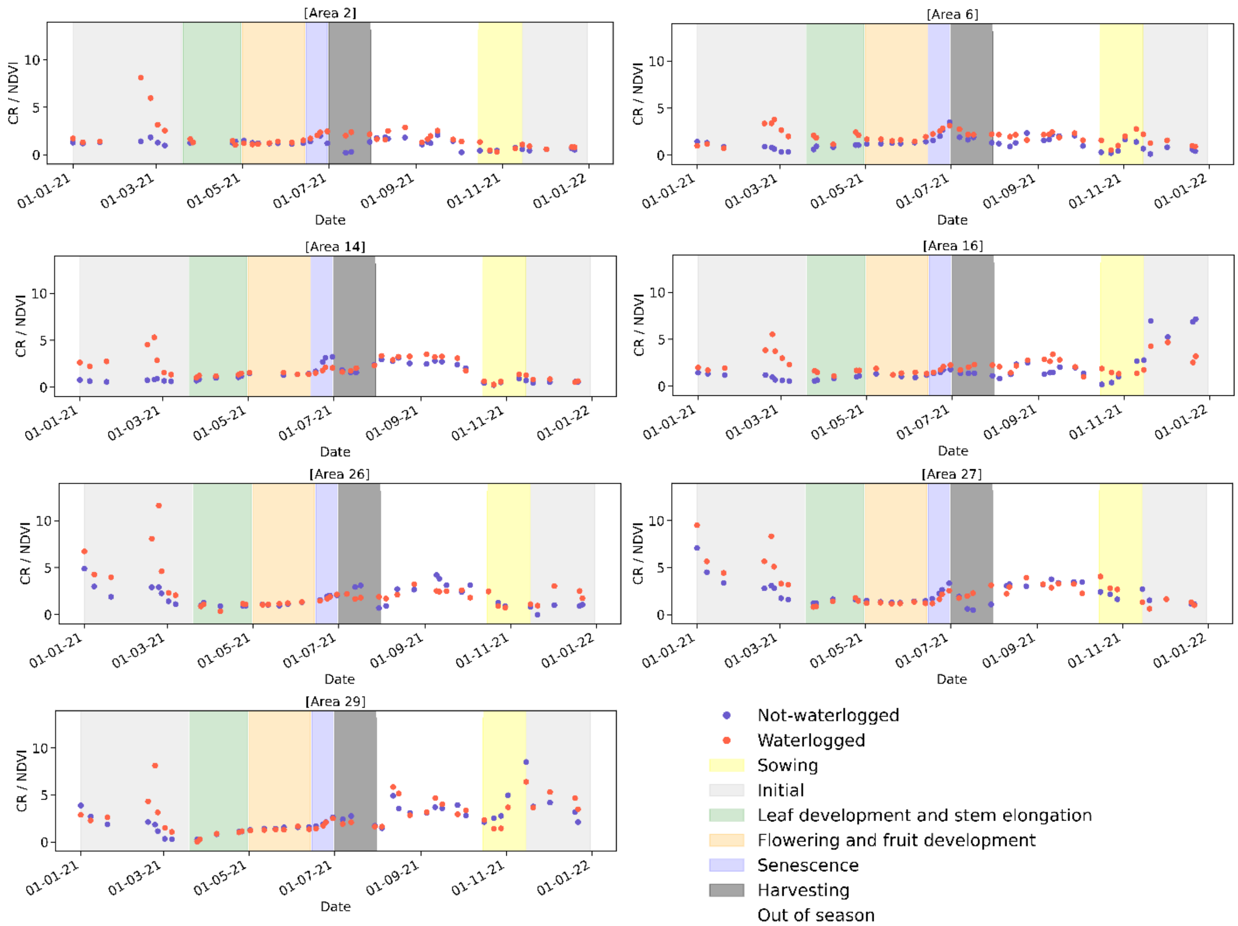

Figure 33: Time series of the ratio of S1 CR (scaled) and S2 NDVI in different wheat fields in Szarvas, Hungary.
NDVI and CR time series for each area is extracted by taking the average of the pixel values located in the part of the field (WL and NWL). As reported in the legend, the colored bar in the background indicates the growth stages from Table 5.

6.5. Mapping spatial patterns of NDVI deviation in NWL and WL locations

Figure 34 maps show the extent and frequency of detected water (column A) and the spatial patterns of NDVI deviation from mean NDVI of NWL locations during different crop growth stages (column B, C, and D). The mean NDVI values from NWL locations for each parcel in different growth stages can be found in Annex B.

In Area 2, the deviation is 0.1 to 0.3 in WL locations on 9th April. On 21st May, the deviation extent has reduced, but the value is the same as on 9th April. The cause of the deviation is the waterlogging as it coincides with the WL locations. The deviation is insignificant in the flowering stage when the plant partially recovers from waterlogging stress. During the senescence stage on 23rd May, winter wheat in the WL location retains chlorophyll longer than in NWL locations due to delayed development, as discussed in section 6.4.2.

In Area 6, the deviation is very high (> 0.5) in WL places. The extent of high deviation (0.3 to 0.5) on 9th April reveals that the extent of the waterlogging impact is much larger than the detected waterlogging extent. On 21st May, the winter wheat in the middle and south-western part of the field shows less deviation (0 to 0.1) than on 9th April as wheat is in the process of recovery in WL locations. The deviation has not changed much in the southern part of the field. On 23rd June, the deviation is negligible as most parts of the field lose chlorophyll due to senescence.

In Area 14, waterlogging appears predominantly in the western part. The larger spatial distribution of the NDVI deviation on the 9th of April reveals that the waterlogging took place in much larger space than detected waterlogging. A very high deviation (> 0.5) is observed in the southern part of the field. The southwestern part of the field with very high NDVI deviation overlaps with the WL part of the field. During the flowering and fruit development stage (21-05-2021), the winter wheat from the WL part did not recover fully, with a maximum deviation of > 0.5. However, on 23rd June, the NWL crop showed healthier status, which can be explained by the decrease of NDVI values of NWL winter wheat during senescence, and late developed WL winter wheat had not gone through senescence at the time of observation.

Long-lasting waterlogging is observed in Area 16. The impact on WL crops is severe, with a deviation of 0.3 to 0.5 and >0.5 on 9th April and 21st May, respectively. The increase in deviation in WL location explains the increasing difference in health status when winter wheat has fully grown. No deviation during the senescence stage implies the loss of chlorophyll in both NWL and WL locations. In Area 26, the impact over WL spots is medium (0.1-0.3) on 9th April and 21st March. This is due to the shorter duration of waterlogging. No discrepancy in NDVI between WL and NWL is found during senescence (23rd June).

Similarly, in Area 27, waterlogging has been detected in the southern part of the field, and the observed damage is medium (0.1-0.3) on 9th April and 21st May. However, on 26th June, less than zero deviation indicates late winter wheat development in WL locations due to waterlogging stress. In Area 29, waterlogging is found on the eastern side of the plot. The deviation of medium to high (0.1-0.5) overlaps with WL spots on 9th April and 21st May. The deviation is higher during the flowering and fruit development stage implies that the growth of winter wheat in WL spot is not as good as NWL wheat. During the senescence (23rd June), the WL wheat plants show higher NDVI than the mean NDVI from NWL locations which explains the late development of WL plants.

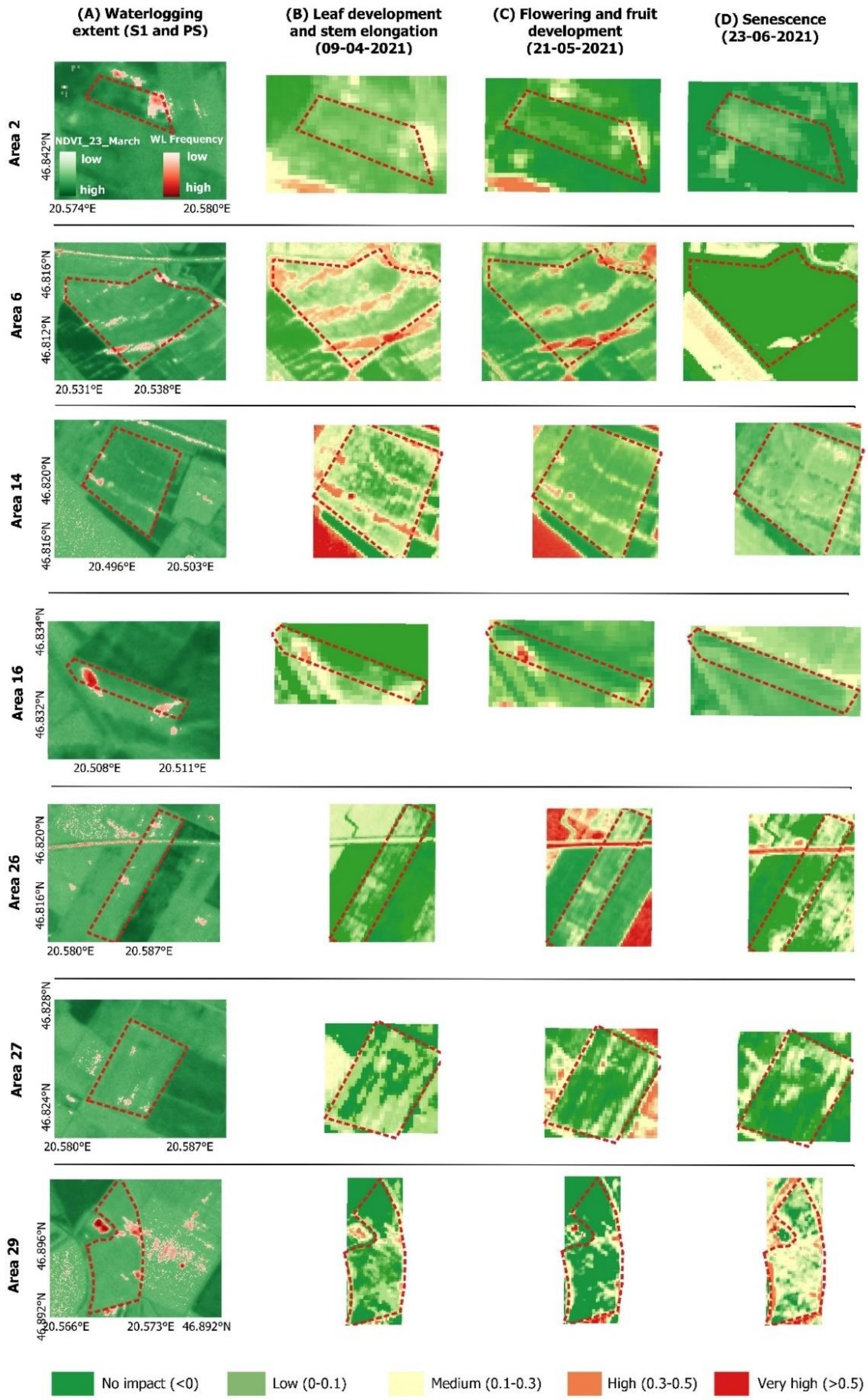

Figure 34: Mapping spatial patterns of NDVI deviation in NWL and WL winter wheat at different growth stages. (A) Waterlogging map for winter wheat parcels derived from S1 and PS. The red color ramp shows observed water frequency. The fields are delineated with the red dash line, and PS NDVI is used as a background. Time series of pixel-level NDVI deviation from Mean NDVI of NWL locations calculated over each parcel for (B) leaf development and stem elongation stage, (C) flowering and fruit development stage, and (D) Senescence. The legend indicates the magnitude of deviation from mean NDVI calculated from NWL locations.

7. CONCLUSIONS AND RECOMMENDATIONS

This chapter includes the conclusion, limitations, and recommendations.

7.1. Conclusion

The overall objective of the study was to detect waterlogging dynamics in agricultural fields and quantify its effect on crop development at different crop growth stages using SAR and optical satellite images. Several S1 and PS images were used to identify WL locations. After that, time series analysis of S1 and S2, as well as synergistic use of S1 and S2, helped to assess the waterlogging impact on crop development throughout different crop growth stages. The conclusions based on the research questions are described below-

RQ1: How can the waterlogging dynamics (occurrence, extent, and timing) be detected using S1 and PS images across the study area?

Waterlogging detection has been done with multitemporal optical (PS) and radar (S1) images. The waterlogging occurred when the winter wheat was just after emergence, so no canopy cover interference made the detection difficult. After sensitivity analysis and employing local knowledge, pixels of NDWI ≥ -0.27 were classified as waterlogged ones, assigning the value 1 to them. All the 15 classified bit maps were then summed up, resulting in a water detection frequency and extent map from PS images.

In radar observations, S1 preprocessed VV images were taken from the same orbit (descending) to reduce errors generating from different view geometries in delineating waterlogging. Speckle filtering was used to reduce the noise from 44 S1 images. Based on a sensitivity analysis, the threshold value of – 16 dB has been applied to separate the WL locations. All the pixels having a value less than the threshold were classified as water pixels, and a waterlogging extent and observed water frequency map has been generated in GEE by adding up all the WL pixels.

It can be assumed that waterlogging may have occurred moments when inconsistencies start between WL and NWL locations. To detect the timing of the waterlogging, the S1 σ^0_{VV} time series have been generated from WL and NWL spots at the intra-field level. Probable waterlogging timing has been marked when VV backscatter from WL and NWL starts to show a difference. In some locations, inconsistencies between σ^0_{VV} values in WL and NWL start from 8th December 2020, and others show differences from 20th January 2021.

RQ2: What are the differences and similarities between waterlogging dynamics detected from S1 and PS images?

Waterlogging from optical images is based on reflectance difference between the water and other features, whereas radar detects water based on the roughness difference between water and other features. The comparisons of waterlogging maps from S1 and PS showed that the spatial extent of waterlogging from S1 images was underestimated. This is attributed to the lower resolution of S1 (10m) than PS (3m). Moreover, the surface roughness is disturbed by the fine sediments deposited by water very slowly and usually becomes muddy instead of smooth water surface. False-negative waterlogging detection by S1 occurs due to mixed pixels when waterlogging appears in narrow patches. Very high-resolution PS showed good waterlogging detection spatially. However, the temporal detection is not the same good due to cloud hindrance, whereas cloud penetration capability allows S1 to capture more consistent temporal detection.

PS detected 3.95% (7.17 km^2) of the area as waterlogging, where S1 spotted 3.76 % (6.83 km^2) of the total area studied.

RQ3: How can crop development be monitored with S1 and S2 images?

The σ^0_{VH}, σ^0_{VV}, CR, and RVI from S1 and NDVI from S2 have been explored for monitoring crop development. In this study, 22 winter wheat fields were selected to observe the change in crop development in different growth stages. To monitor crop development, the temporal profiles of average σ^0_{VH}, σ^0_{VV}, CR, RVI, and NDVI for all the winter wheat parcels were extracted by averaging values from all pixels within the field boundary. The change in σ^0_{VH}, σ^0_{VV}, CR, RVI, and NDVI values during different crop growth stages were analyzed and discussed with reference to the physical change of crop in all growth stages.

RQ4: How do cross-ratio CR, RVI, and NDVI derived from S1 and S2 vary in different crop growth stages?

NDVI is sensitive to chlorophyll which changes over different growth stages of crops, whereas CR and RVI are sensitive to VWC as well as the structure of leaves and stems, which is an indicator of crop biomass. From March, NDVI starts to increase, whereas the start of the increase in RVI and CR is noticed in April. The earlier increase in NDVI is due to the sensitivity to the chlorophyll activity of the growing winter wheat. However, CR and RVI are dominated by VWC and the plant's canopy, which is negligible when winter wheat is short and sparsely distributed. The surface roughness and soil moisture mainly control the CR and RVI values in this growth stage. During the leaf development and stem elongation stage, NDVI, CR, and RVI sharply increase due to the increase in chlorophyll activity, VWC, leaves, and stems. At the beginning of June, the highest values are observed of the NDVI, CR, and RVI when winter wheat plants have fully grown. During the senescence (late June), NDVI drops sharply as the plant starts to lose chlorophyll. CR and RVI started to decline later and more gradually than NDVI as winter wheat was holding VWC even though there was no photosynthesis activity.

RQ5: What is the impact of waterlogging observed in different crop growth stages using the S1 and S2 time series?

S2 NDVI from WL locations shows lower values (0.1-0.2 difference) than NWL locations during the initial stage, which indicates less canopy density due to waterlogging impact. Moreover, there was a systematic drop in NDVI in all WL locations as the places were underwater during the WL period (section 6.4.2). A clear difference with lower NDVI in WL locations is observed when plants go through leaf development and stem elongation in April. The highest NDVI differences (up to 0.4) are noticed during flowering and fruit development (May to mid-June) when chlorophyll activity in winter wheat stabilizes. During the senescence stage, NDVI shows less difference (<0.1) in WL and NWL locations. However, NDVI in NWL spots loses greenness earlier than in WL locations. This is due to the slower development of winter wheat due to waterlogging stress. This has resulted in slightly higher NDVI in WL locations during senescence. After harvesting, a slight rise in NDVI in WL locations is due to the emergence of weeds and grass.

On the other hand, CR and RVI do not show much difference between WL and NWL locations during the initial stage due to the dominance of CR and RVI values from the soil surface. During leaf development and stem elongation stage in April, CR shows slightly lower values (2-3 dB) in WL locations as less biomass is developed in the WL crop. Similar to NDVI, the highest differences in CR and RVI between WL and NWL locations are found during April, when winter wheat shows the maximum growth.

During senescence, the CR and RVI differences between the WL and NWL locations start to decrease, and after harvest, there is a rise in CR and RVI in WL spots due to the growth of weeds or grass attracted by higher soil moisture.

RQ6: How can the difference in crop development be evaluated in WL and NWL crops by combining S1 and S2?

The difference in the ratio of CR and NDVI between WL and NWL is found between January and March, where a significant inconsistency in CR is observed in February due to waterlogging. During this time, the CR does not show good agreement to NDVI in WL locations as CR is very sensitive to waterlogging. When wheat plants start to grow, NDVI increases in response to winter wheat development earlier than CR. From leaf development and stem elongation to flowering and fruit development stages, both NDVI and CR have similar responses to crop development in both waterlogging states, which is reflected in the ratio of NDVI and CR. However, some discrepancies between NWL and WL locations are visible during the senescence and after harvesting. These inconsistencies are related to the difference in the rate of structural change as well as VWC and chlorophyll loss in NWL and WL winter wheat during senescence. After the crop is harvested, a rise in NDVI and CR is found due to the emergence of weeds or grass and high soil water content in WL locations

RQ7: What is the spatial pattern of NDVI deviation in NWL and WL locations in different growth stages at the intra-field level?

Results show that higher spatial deviation in NDVI in WL locations during leaf development and stem elongation stage (9th April) in WL spots. During this time, chlorophyll activity usually increases, but this activity is hindered in the WL wheat plant, resulting in a high NDVI deviation from NDVI from NWL locations (Figure 34B). The highest deviation in WL spots is noticeable during the flowering and fruit development stage (starting from late May), when wheat shows the highest NDVI values (Figure 34C). During senescence, WL wheat showed higher NDVI values than NWL, indicating that plants stressed by waterlogging developed later. So, NWL plants were losing greenness due to senescence, and at the same time, WL plants were holding chlorophyll because of delayed growth (Figure 34D).

To conclude, waterlogging detection with PS is different from S1 detection. PS can detect small waterlogged locations, and S1 can observe waterlogging even on cloudy days. S2-derived NDVI shows an early increase and decrease than S1-derived CR and RVI while monitoring winter wheat development due to differences in sensitivity to chlorophyll and biomass. The highest difference in NDVI, CR, and RVI is noticeable during the flowering and fruit development stage between WL and NWL locations when winter wheat shows maximum growth. A delay in winter wheat development is evident with NDVI, CR, and RVI. The ratio of NDVI and CR reveals that most differences between WL and NWL locations are found during the initial stage since CR is sensitive to waterlogging and NDVI is not. Some slight inconsistencies between WL and NWL locations are found at the beginning of March and the end of June. This can be attributed to the difference in the rate of increase and decrease of biomass and chlorophyll resulted in poor agreement between CR and NDVI from WL and NWL winter wheat. The spatial patterns of NDVI deviation illustrate that high and very high deviations coincide with the WL locations. The deviation is the highest during the flowering and fruit development stage and when the waterlogging duration is longer.

7.2. Limitations and recommendations

There are some uncertainties and limitations involved in this study which can be translated into recommendations for future research. Few recommendations are also made for future studies based on the conclusion of this study.

- Waterlogging maps have been created by thresholding of satellite data. The applied threshold values were based on remote sensing assisted by field-visit, local expert knowledge, and visual inspection of high-resolution satellite images. There is a high chance of having a few false positive and false negative waterlogging pixels due to limited field information. A detailed validation study can be carried out in the future for more accurate waterlogging maps.

- Topographic analysis such as Height Above the Nearest Drainage (HAND) with a very high-resolution DEM could improve the accuracy and reliability of the waterlogging map.

- Soil moisture variation in the waterlogged and non-waterlogged spots at the intra-field level should be studied further. Linking it to the satellite information can reveal timely waterlogging stress detection using remote sensing.

- For this study, only the winter wheat crop was considered in studying the impact of waterlogging. However, how tolerant other crops are to waterlogging should also be explored.

- Yield and crop biomass data can be used to quantify crop damage due to waterlogging at different growth stages and observe how they correlate with the impact found from satellite observation.

- For this study, the crop phenological stage with an approximate timeframe was used, which is one of the limitations of the study. A detailed land surface phenology with the exact date of events would help to understand the waterlogging impact on crops more comprehensively.

- Waterlogging maps and crop development information extracted from satellite data can be used to create dynamic thresholding of vegetation indices at different phenological stages to extract damaged areas for more informed decision-making on crop management by the farmers.

8. REFERENCE

Allen, R., Pereira, L., Raes, D., & Smith, M. (2006). Crop evapotranspiration - Guidelines for computing crop water requirements. *FAO - Food and Agriculture Organization of the United Nations*, 48.

Barreto, S., Bártfai, B., Engloner, A., Liptay, Árpád Zoltán Madarász, T., & Márta, V. (2017). Water in Hungary. *National Water Programme of the Hungarian Academy of Sciences*, *June*, 97.

Beck, H. E., Zimmermann, N. E., McVicar, T. R., Vergopolan, N., Berg, A., & Wood, E. F. (2018). Present and future Köppen-Geiger climate classification maps at 1-km resolution. *Scientific Data 2018 5:1*, *5*(1), 1–12. https://doi.org/10.1038/sdata.2018.214

Betbeder, J., Rapinel, S., Corpetti, T., Pottier, E., Corgne, S., & Hubert-Moy, L. (2014). Multitemporal classification of TerraSAR-X data for wetland vegetation mapping. *Journal of Applied Remote Sensing*, *8*(1), 083648. https://doi.org/10.1117/1.jrs.8.083648

Boori, M. S., Choudhary, K., Paringer, R., Sharma, A. K., Kupriyanov, A., & Corgne, S. (2019). Monitoring crop phenology using NDVI time series from sentinel 2 satellite data. *2019 5th International Conference on Frontiers of Signal Processing, ICFSP 2019*, 62–66. https://doi.org/10.1109/ICFSP48124.2019.8938078

Bourgeau-Chavez, L. L., Riordan, K., Powell, R. B., Miller, N., & Nowels, M. (2009). Improving wetland characterization with multi-sensor, multi-temporal SAR and optical/infrared data fusion. *Advances in Geoscience and Remote Sensing*. https://doi.org/10.5772/8327

Brahmabhatt, V. S., Dalwadi, G. B., Chhabra, S. B., Ray, S. S., & Dadhwal, V. K. (2000). Land Use/Land Cover change mapping in Mahi canal command area, Gujarat, using multi-temporal satellite data. *Journal of the Indian Society of Remote Sensing 2000 28:4*, *28*(4), 221–232. https://doi.org/10.1007/BF02990813

Brown, S. C. M., Quegan, S., Morrison, K., Bennett, J. C., & Cookmartin, G. (2003). High-resolution measurements of scattering in wheat canopies - Implications for crop parameter retrieval. *IEEE Transactions on Geoscience and Remote Sensing*, *41*(7 PART I), 1602–1610. https://doi.org/10.1109/TGRS.2003.814132

Carlson, T. N., Gillies, R. R., & Perry, E. M. (1994). A method to make use of thermal infrared temperature and NDVI measurements to infer surface soil water content and fractional vegetation cover. *Remote Sensing Reviews*, *9*(1–2), 161–173. https://doi.org/10.1080/02757259409532220

Chen, H., Zeng, W., Jin, Y., Zha, Y., Mi, B., & Zhang, S. (2020). Development of a waterlogging analysis system for paddy fields in irrigation districts. *Journal of Hydrology*, *591*, 125325. https://doi.org/10.1016/J.JHYDROL.2020.125325

Choubey, V. K. (1997). Detection and delineation of waterlogging by remote sensing techniques. *Journal of the Indian Society of Remote Sensing 1997 25:2*, *25*(2), 123–135. https://doi.org/10.1007/BF03025910

Choudhury, B. J. (1989). Monitoring global land surface using Nimbus-7 37 GHz data: Theory and examples. *International Journal of Remote Sensing*, *10*(10), 1579–1605. https://doi.org/10.1080/01431168908903993

Chowdary, V. M., Chandran, R. V., Neeti, N., Bothale, R. V., Srivastava, Y. K., Ingle, P., Ramakrishnan, D., Dutta, D., Jeyaram, A., Sharma, J. R., & Singh, R. (2008). Assessment of surface and sub-surface waterlogged areas in irrigation command areas of Bihar state using remote sensing and GIS. *Agricultural Water Management*, *95*(7), 754–766. https://doi.org/10.1016/J.AGWAT.2008.02.009

Costa, M. P. F., Niemann, O., Novo, E., & Ahern, F. (2002). Biophysical properties and mapping of aquatic vegetation during the hydrological cycle of the Amazon floodplain using JERS-1 and Radarsat. *International Journal of Remote Sensing*, *23*(7), 1401–1426. https://doi.org/10.1080/01431160110092957

De Jeu, R. A. M., Holmes, T. R. H., Parinussa, R. M., & Owe, M. (2014). A spatially coherent global soil moisture product with improved temporal resolution. *Journal of Hydrology*, *516*, 284–296. https://doi.org/10.1016/J.JHYDROL.2014.02.015

den Besten, N., Steele-Dunne, S., de Jeu, R., & van der Zaag, P. (2021). Towards monitoring waterlogging with remote sensing for sustainable irrigated agriculture. *Remote Sensing*, *13*(15), 2929. https://doi.org/10.3390/rs13152929

Dwivedi, R. S., Rao, B. R. M., & Bhattacharya, S. (1999). Mapping wetlands of the sundaban delta and it‘s environs using ers-1 sar data. *International Journal of Remote Sensing*, *20*(11), 2235–2247. https://doi.org/10.1080/014311699212227

EU-DEM. (2017). Digital Elevation Model Over Europe [WWW Document]. https://www.eea.europa.eu/data-and-maps/data/copernicus-land-monitoring-service-eu-dem

Ferrazzoli, P., Paloscia, S., Pampaloni, P., Schiavon, G., Solimini, D., & Coppo, P. (1992). Sensitivity of microwave measurements to vegetation biomass and soil moisture content: a case study. *IEEE Transactions on Geoscience and Remote Sensing*, *30*(4), 750–756. https://doi.org/10.1109/36.158869

Gorelick, N., Hancher, M., Dixon, M., Ilyushchenko, S., Thau, D., & Moore, R. (2017). Google Earth Engine: Planetary-scale geospatial analysis for everyone. *Remote Sensing of Environment*, *202*, 18–27. https://doi.org/10.1016/J.RSE.2017.06.031

Hamilton, S. K., Sippel, S. J., & Melack, J. M. (1996). Inundation patterns in the Pantanal wetland of South America determined from passive microwave remote sensing. *Archiv Fur Hydrobiologie*, *137*(1), 1–23. https://doi.org/10.1127/ARCHIV-HYDROBIOL/137/1996/1

Hess, L. L., Melack, J. M., Melack, J. M., Filoso, S., Wang, Y., & Wang, Y. (1995). Delineation of inundated area and vegetation along the Amazon floodplain with the SIR-C synthetic aperture radar. *IEEE Transactions on Geoscience and Remote Sensing*, *33*(4), 896–904. https://doi.org/10.1109/36.406675

Hess, L. L., Melack, J. M., Novo, E. M. L. M., Barbosa, C. C. F., & Gastil, M. (2003). Dual-season mapping of wetland inundation and vegetation for the central Amazon basin. *Remote Sensing of Environment*, *87*(4), 404–428. https://doi.org/10.1016/J.RSE.2003.04.001

Hess, L. L., Melack, J. M., & Simonett, D. S. (1990). Radar detection of flooding beneath the forest canopy: A review. *International Journal of Remote Sensing*, *11*(7), 1313–1325. https://doi.org/10.1080/01431169008955095

Houborg, R., & McCabe, M. F. (2016). High-resolution NDVI from Planet's constellation of earth observing nano-satellites: A new data source for precision agriculture. *Remote Sensing 2016, Vol. 8, Page 768*, *8*(9), 768. https://doi.org/10.3390/RS8090768

Huang, H., & Roy, D. P. (2021). Characterization of Planetscope-0 Planetscope-1 surface reflectance and normalized difference vegetation index continuity. *Science of Remote Sensing*, *3*, 100014. https://doi.org/10.1016/J.SRS.2021.100014

Irfan, M., Hayat, S., Hayat, Q., Afroz, S., & Ahmad, A. (2010). Physiological and biochemical changes in plants under waterlogging. *Protoplasma*, *241*(1–4), 3–17. https://doi.org/10.1007/s00709-009-0098-8

ITC. (2019). *ITC satellites and sensors database*. University of Twente.

https://webapps.itc.utwente.nl/sensor/default.aspx?view=allsatellites

JRC-MARS. (2015). *Crop calenders*. https://agri4cast.jrc.ec.europa.eu/DataPortal/Index.aspx?rid=23&o=sd

Kandus, P., Pulz, T., Parmuchi, G., & Bava, I. (2014). Influence of flood conditions and vegetation status on the radar backscatter of wetland ecosystems. *Https://Doi.Org/10.1080/07038992.2001.10854907*, *27*(6), 663–668. https://doi.org/10.1080/07038992.2001.10854907

Karoly, B., Teodora, B., Balazs, B., & Brikic, M. (2013). *Inland excess water* (S. József & Z. Leeuwen, Boudewijn Van Tobak (Eds.)). Szegedi Tudományegyetem TTIK Természeti Földrajzi és Geoinformatikai Tanszék. http://jlevente.com/publications/SzatmariVanLeeuwen_Inland_Excess_Water.pdf

Kasischke, E. S., Smith, K. B., Bourgeau-Chavez, L. L., Romanowicz, E. A., Brunzell, S., & Richardson, C. J. (2003). Effects of seasonal hydrologic patterns in south Florida wetlands on radar backscatter measured from ERS-2 SAR imagery. *Remote Sensing of Environment*, *88*(4), 423–441. https://doi.org/10.1016/J.RSE.2003.08.016

Kaur, G., Singh, G., Motavalli, P. P., Nelson, K. A., Orlowski, J. M., & Golden, B. R. (2020). Impacts and management strategies for crop production in waterlogged or flooded soils: A review. *Agronomy Journal*, *112*(3), 1475–1501. https://doi.org/10.1002/AGJ2.20093

Khabbazan, S., Vermunt, P., Steele-Dunne, S., Arntz, L. R., Marinetti, C., van der Valk, D., Iannini, L., Molijn, R., Westerdijk, K., & van der Sande, C. (2019). Crop monitoring using Sentinel-1 data: A case study from The Netherlands. *Remote Sensing*, *11*(16), 1887. https://doi.org/10.3390/rs11161887

Khadka, A. (2018). Integrating remote sensing and infiltration model to analyze the ponding dynamics in Hungary. *Universtiy of Twente, Faculty of Geoinformation Science and Earth Observation.*, 59. http://essay.utwente.nl/83327/

Khaldoune, J., Van Bochove, E., Bernier, M., & Nolin, M. C. (2011). Mapping agricultural frozen soil on the watershed scale using remote sensing data. *Applied and Environmental Soil Science*, *2011*, 1–16. https://doi.org/10.1155/2011/193237

Kim, Y., & Van Zyl, J. J. (2009). A time-series approach to estimate soil moisture using polarimetric radar data. *IEEE Transactions on Geoscience and Remote Sensing*, *47*(8), 2519–2527. https://doi.org/10.1109/TGRS.2009.2014944

Kumar, D., Rao, S., & Sharma, J. (2013). Radar vegetation index as an alternative to NDVI for monitoring of soyabean and cotton. *Indian Cartographer*, *XXXIII*. http://earthexplorer.usgs.gov/

Kwoun, O. I., & Lu, Z. (2009). Multi-temporal RADARSAT-1 and ERS backscattering signatures of coastal wetlands in southeastern louisiana. *Photogrammetric Engineering and Remote Sensing*, *75*(5), 607–617. https://doi.org/10.14358/PERS.75.5.607

Lajos, M. (2009). *Alkalmazott hidrogeológia*.

Lang, M. W., Townsend, P. A., & Kasischke, E. S. (2008). Influence of incidence angle on detecting flooded forests using C-HH synthetic aperture radar data. *Remote Sensing of Environment*, *112*(10), 3898–3907. https://doi.org/10.1016/J.RSE.2008.06.013

Lenney, M. P., Woodcock, C. E., Collins, J. B., & Hamdi, H. (1996). The status of agricultural lands in Egypt: The use of multitemporal NDVI features derived from landsat TM. *Remote Sensing of Environment*, *56*(1), 8–20. https://doi.org/10.1016/0034-4257(95)00152-2

Lillesand, T., Kiefer, R., & Chipman, J. (2015). Remote sensing and image interpretation Seventh Ed. *John Wiley and Sons, Inc., New York*, 736. https://www.wiley.com/enus/Remote+Sensing+and+Image+Interpretation%2C+7th+Edition-p-9781118343289

Linkemer, G., Board, J. E., & Musgrave, M. E. (1998). Waterlogging effects on growth and yield components in late-planted soybean. *Crop Science*, *38*(6), 1576–1584. https://doi.org/10.2135/cropsci1998.0011183X003800060028x

Liu, Y. (2012). Why NDWI threshold varies in delineating water body from multitemporal images? *International Geoscience and Remote Sensing Symposium (IGARSS)*, 4375–4378. https://doi.org/10.1109/IGARSS.2012.6350404

Lopez-Sanchez, J. M., Vicente-Guijalba, F., David Ballester-Berman, J., & Cloude, S. R. (2013). Estimating phenology of agricultural crops from space. *ESA Living Planet Symposium 2013*, *SP-722*, 1–8. https://pdfs.semanticscholar.org/25f2/8cff78375459a08681ef03e94a14380fcf2a.pdf

Mandal, A. K., & Sharma, R. C. (2001). Mapping of waterlogged areas and salt affected soils in the IGNP command area. *Journal of the Indian Society of Remote Sensing 2001 29:4*, *29*(4), 229–235. https://doi.org/10.1007/BF02995728

Markert, K. N., Markert, A. M., Mayer, T., Nauman, C., Haag, A., Poortinga, A., Bhandari, B., Thwal, N. S., Kunlamai, T., Chishtie, F., Kwant, M., Phongsapan, K., Clinton, N., Towashiraporn, P., & Saah, D. (2020). Comparing Sentinel-1 surface water mapping algorithms and radiometric terrain correction processing in southeast Asia utilizing Google Earth Engine. *Remote Sensing*, *12*(15), 2469. https://doi.org/10.3390/RS12152469

Marti-Cardona, B., Lopez-Martinez, C., Dolz-Ripolles, J., & Bladè-Castellet, E. (2010). ASAR polarimetric, multi-incidence angle and multitemporal characterization of Doñana wetlands for flood extent monitoring. *Remote Sensing of Environment*, *114*(11), 2802–2815. https://doi.org/10.1016/J.RSE.2010.06.015

Marti, J., Savin, R., & Slafer, G. A. (2015). Wheat yield as affected by length of exposure to waterlogging during stem elongation. *Journal of Agronomy and Crop Science*, *201*(6), 473–486. https://doi.org/10.1111/jac.12118

Martinis, S., & Rieke, C. (2015). Backscatter analysis using multi-temporal and multi-frequency SAR data in the context of flood mapping at River Saale, Germany. *Remote Sensing*, *7*(6), 7732–7752. https://doi.org/10.3390/rs70607732

Mc Nairn, H., Hochheim, K., & Rabe, N. (2004). Applying polarimetric radar imagery for mapping the productivity of wheat crops. *Canadian Journal of Remote Sensing*, *30*(3), 517–524. https://doi.org/10.5589/m03-068

McFeeters, S. K. (1996). The use of the Normalized Difference Water Index (NDWI) in the delineation of open water features. *International Journal of Remote Sensing*, *17*(7), 1425–1432. https://doi.org/10.1080/01431169608948714

Meier, U., Feller, C., Bleiholder, H., Frau, E., Hess, M., Wicke, H., van den Boom, T., Stauss, R., Klose, R., Hack, H., Buhr, L., & Lancashire, P. D. (2018). Growth stages of mono- and dicotyledonous plants: BBCH Monograph. *Federal Biological Research Centre for Agriculture and Forestry*, 204. https://doi.org/10.5073/20180906-074619

Meroni, M., d'Andrimont, R., Vrieling, A., Fasbender, D., Lemoine, G., Rembold, F., Seguini, L., & Verhegghen, A. (2021). Comparing land surface phenology of major European crops as derived from SAR and multispectral data of Sentinel-1 and -2. *Remote Sensing of Environment*, *253*, 112232. https://doi.org/10.1016/J.RSE.2020.112232

Mezősi, G. (2017). The physical geography of Hungary. *Springer International Publishing: Basel, Switzerland.* https://doi.org/10.1007/978-3-319-45183-1

Mezősi, G., Blanka, V., Bata, T., Kovacs, F., & Meyer, B. (2015). Estimation of regional differences in wind erosion sensitivity in Hungary. *Natural Hazards and Earth System Sciences*, *15*(1), 97–107. https://doi.org/10.5194/nhess-15-97-2015

Mishra, V., Limaye, A. S., Muench, R. E., Cherrington, E. A., & Markert, K. N. (2020). Evaluating the performance of high-resolution satellite imagery in detecting ephemeral water bodies over West Africa. *International Journal of Applied Earth Observation and Geoinformation*, *93*, 102218. https://doi.org/10.1016/J.JAG.2020.102218

Mosleh, M. K., Hassan, Q. K., & Chowdhury, E. H. (2015). Application of remote sensors in mapping rice area and forecasting its production: A review. In *Sensors (Switzerland)* (Vol. 15, Issue 1, pp. 769–791). MDPI AG. https://doi.org/10.3390/s150100769

Mougin, E., Proisy, C., Marty, G., Fromard, F., Puig, H., Betoulle, J. L., & Rudant, J. P. (1999). Multifrequency and multipolarization radar backscattering from mangrove forests. *IEEE Transactions on Geoscience and Remote Sensing*, *37*(1 PART 1), 94–102. https://doi.org/10.1109/36.739128

Mullissa, A., Vollrath, A., Odongo-Braun, C., Slagter, B., Balling, J., Gou, Y., Gorelick, N., & Reiche, J. (2021). Sentinel-1 SAR backscatter analysis ready data preparation in Google Earth Engine. *Remote Sensing*, *13*(10), 1954. https://doi.org/10.3390/rs13101954

Nasirzadehdizaji, R, Akyuz, D. E., & Cakir, Z. (2019). Flood mapping and permanent water bodies change detection using sentinel sar data. *International Archives of the Photogrammetry, Remote Sensing and Spatial Information Sciences - ISPRS Archives*, *42*(4/W18), 797–801. https://doi.org/10.5194/isprs-archives-XLII-4-W18-797-2019

Nasirzadehdizaji, Rouhollah, Sanli, F. B., Abdikan, S., Cakir, Z., Sekertekin, A., & Ustuner, M. (2019). Sensitivity analysis of multi-temporal Sentinel-1 SAR parameters to crop height and canopy coverage. *Applied Sciences (Switzerland)*, *9*(4), 655. https://doi.org/10.3390/app9040655

Ovakoglou, G., Cherif, I., Alexandridis, T. K., Pantazi, X.-E., Tamouridou, A.-A., Moshou, D., Tseni, X., Raptis, I., Kalaitzopoulou, S., & Mourelatos, S. (2021). Automatic detection of surface-water bodies from Sentinel-1 images for effective mosquito larvae control. *Journal of Applied Remote Sensing*, *15*(01), 014507. https://doi.org/10.1117/1.jrs.15.014507

Owe, M., De Jeu, R., & Walker, J. (2001). A methodology for surface soil moisture and vegetation optical depth retrieval using the microwave polarization difference index. *IEEE Transactions on Geoscience and Remote Sensing*, *39*(8), 1643–1654. https://doi.org/10.1109/36.942542

Owe, Manfred, Jeu, R. de, & Holmes, T. (2008). Multisensor historical climatology of satellite-derived global land surface moisture. *Journal of Geophysical Research: Earth Surface*, *113*(F1), 1002. https://doi.org/10.1029/2007JF000769

Pálfai, I. (2011). Precipitation conditions and excess water formation (in Hungarian). *Hungarian Hydrological Society, 29th National Meeting.* http://www.hidrologia.hu/vandorgyules/29/dolgozatok/palfai_imre.html

Pantaleoni, E., Engel, B. A., & Johannsen, C. J. (2007). Identifying agricultural flood damage using Landsat imagery. *Precision Agriculture*, *8*(1–2), 27–36. https://doi.org/10.1007/s11119-006-9026-5

Parker, M. (2010). Radar basics. In *Digital Signal Processing 101* (pp. 191–200). Newnes. https://doi.org/10.1016/b978-1-85617-921-8.00020-1

Pásztor, L., Körösparti, J., Bozán, C., Laborczi, A., & Takács, K. (2015a). Spatial risk assessment of hydrological extremities: Inland excess water hazard, Szabolcs-Szatmár-Bereg County, Hungary. *Journal of Maps*, *11*(4), 636–644. https://doi.org/10.1080/17445647.2014.954647

Pásztor, L., Körösparti, J., Bozán, C., Laborczi, A., & Takács, K. (2015b). Spatial risk assessment of hydrological extremities: Inland excess water hazard, Szabolcs-Szatmár-Bereg County, Hungary. *Journal of Maps*, *11*(4), 636–644. https://doi.org/10.1080/17445647.2014.954647

Pásztor, L., Laborczi, A., Bakacsi, Z., Szabó, J., & Illés, G. (2018). Compilation of a national soil-type map for Hungary by sequential classification methods. *Geoderma*, *311*, 93–108. https://doi.org/10.1016/j.geoderma.2017.04.018

Pásztor, L., Pálfai, I., Bozán, C., Kőrösparti, J., Szabó, J., Bakacsi, Z., & Kuti, L. (2006). *Spatial stochastic modelling of inland inundation hazard*.

Pekel, J. F., Cottam, A., Gorelick, N., & Belward, A. S. (2016). High-resolution mapping of global surface water and its long-term changes. *Nature*, *540*(7633), 418–422. https://doi.org/10.1038/nature20584

Picard, G., Le Toan, T., & Mattia, F. (2003). Understanding C-band radar backscatter from wheat canopy using a multiple-scattering coherent model. *IEEE Transactions on Geoscience and Remote Sensing*, *41*(7 PART I), 1583–1591. https://doi.org/10.1109/TGRS.2003.813353

Pierdicca, N., Pulvirenti, L., Chini, M., Guerriero, L., & Candela, L. (2013). Observing floods from space: Experience gained from COSMO-SkyMed observations. *Acta Astronautica*, *84*, 122–133. https://doi.org/10.1016/J.ACTAASTRO.2012.10.034

Planet Labs. (2022). *Planet imagery product specifications* . https://assets.planet.com/docs/Planet_Combined_Imagery_Product_Specs_letter_screen.pdf

Pope, K. O., Rejmankova, E., Paris, J. F., & Woodruff, R. (1997). Detecting seasonal flooding cycles in marshes of the Yucatan Peninsula with SIR-C polarimetric radar imagery. *Remote Sensing of Environment*, *59*(2), 157–166. https://doi.org/10.1016/S0034-4257(96)00151-4

Prigent, C., Jimenez, C., & Bousquet, P. (2020). Satellite-derived global surface water extent and dynamics over the last 25 Years (GIEMS-2). *Journal of Geophysical Research: Atmospheres*, *125*(3), e2019JD030711. https://doi.org/10.1029/2019JD030711

Prigent, Catherine, Aires, F., Rossow, W., & Matthews, E. (2001). Joint characterization of vegetation by satellite observations from visible to microwave wavelengths: A sensitivity analysis. *Journal of Geophysical Research Atmospheres*, *106*(D18), 20665–20685. https://doi.org/10.1029/2000JD900801

Pulvirenti, L., Chini, M., Pierdicca, N., Guerriero, L., & Ferrazzoli, P. (2011). Flood monitoring using multi-temporal COSMO-SkyMed data: Image segmentation and signature interpretation. *Remote Sensing of Environment*, *115*(4), 990–1002. https://doi.org/10.1016/J.RSE.2010.12.002

Pulvirenti, L., Pierdicca, N., Chini, M., & Guerriero, L. (2011). An algorithm for operational flood mapping from Synthetic Aperture Radar (SAR) data using fuzzy logic. *Natural Hazards and Earth System Science*, *11*(2), 529–540. https://doi.org/10.5194/nhess-11-529-2011

Pulvirenti, Luca, Pierdicca, N., Chini, M., & Guerriero, L. (2013). Monitoring flood evolution in vegetated areas using cosmo-skymed data: The tuscany 2009 case study. *IEEE Journal of Selected Topics in Applied Earth Observations and Remote Sensing*, *6*(4), 1807–1816. https://doi.org/10.1109/JSTARS.2012.2219509

Richards, J. A., Woodgate, P. W., & Skidmore, A. K. (1987). An explanation of enhanced radar backscattering from flooded forests. *International Journal of Remote Sensing*, *8*(7), 1093–1100. https://doi.org/10.1080/01431168708954756

Ritzema, H. P. (2016). Drain for gain: Managing salinity in irrigated lands—A review. *Agricultural Water Management*, *176*, 18–28. https://doi.org/10.1016/J.AGWAT.2016.05.014

Ritzema, H. P., Satyanarayana, T. V., Raman, S., & Boonstra, J. (2008). Subsurface drainage to combat waterlogging and salinity in irrigated lands in India: Lessons learned in farmers' fields. *Agricultural Water Management*, *95*(3), 179–189. https://doi.org/10.1016/J.AGWAT.2007.09.012

Rodrigues, G. C., & Braga, R. P. (2021). Evaluation of nasa power reanalysis products to estimate daily weather variables in a hot summer mediterranean climate. *Agronomy*, *11*(6), 1–17. https://doi.org/10.3390/agronomy11061207

Rouse, J. W., Haas, R. H., Schell, J. A., & Deering, D. W. (1974). Monitoring vegetation systems in the Great Plains with ERTS - NASA Technical Reports Server (NTRS). *NASA. Goddard Space Flight Center 3d ERTS-1 Symp., Vol. 1, Sect. A*, 309–351. https://ntrs.nasa.gov/citations/19740022614

Roy, D. P., Huang, H., Houborg, R., & Martins, V. S. (2021). A global analysis of the temporal availability of PlanetScope high spatial resolution multi-spectral imagery. *Remote Sensing of Environment*, *264*, 112586. https://doi.org/10.1016/J.RSE.2021.112586

Sairam, R. K., Kumutha, D., Ezhilmathi, K., Deshmukh, P. S., & Srivastava, G. C. (2008). Physiology and biochemistry of waterlogging tolerance in plants. *Biologia Plantarum 2008 52:3*, *52*(3), 401–412. https://doi.org/10.1007/S10535-008-0084-6

Sang, H., Zhang, J., Lin, H., & Zhai, L. (2014). Multi-polarization ASAR backscattering from herbaceous wetlands in poyang lake region, China. *Remote Sensing*, *6*(5), 4621–4646. https://doi.org/10.3390/rs6054621

Sasidharan, R., & Voesenek, L. A. C. J. (2015). Ethylene-mediated acclimations to flooding stress. *Plant Physiology*, *169*(1), 3–12. https://doi.org/10.1104/pp.15.00387

Savitzky, A., & Golay, M. J. E. (1964). Smoothing and differentiation of data by simplified least squares procedures. *Analytical Chemistry*, *36*(8), 1627–1639. https://doi.org/10.1021/ac60214a047

Scherer, D., Hall, D. K., Hochschild, V., König, M., Winther, J. G., Duguay, C. R., Pivot, F., Mätzler, C., Rau, F., Seidel, K., Solberg, R., & Walker, A. E. (2005). Remote sensing of snow cover. In *Geophysical Monograph Series* (Vol. 163, pp. 7–38). American Geophysical Union. https://doi.org/10.1029/163GM03

Shaw, R. E., Meyer, W. S., McNeill, A., & Tyerman, S. D. (2013). Waterlogging in Australian agricultural landscapes: A review of plant responses and crop models. In *Crop and Pasture Science* (Vol. 64, Issue 6, pp. 549–562). https://doi.org/10.1071/CP13080

Sippe, S. J., Hamilton, S. K., Melack, J. M., & Novo, E. M. M. (1998a). Passive microwave observations of inundation area and the area/stage relation in the amazon river floodplain. *International Journal of Remote Sensing*, *19*(16), 3055–3074. https://doi.org/10.1080/014311698214181

Sippe, S. J., Hamilton, S. K., Melack, J. M., & Novo, E. M. M. (1998b). Passive microwave observations of inundation area and the area/stage relation in the amazon river floodplain. *International Journal of Remote Sensing*, *19*(16), 3055–3074. https://doi.org/10.1080/014311698214181

Souza-Filho, P. W. M., Paradella, W. R., Rodrigues, S. W. P., Costa, F. R., Mura, J. C., & Gonçalves, F. D. (2011). Discrimination of coastal wetland environments in the Amazon region based on multi-polarized L-band airborne Synthetic Aperture Radar imagery. *Estuarine, Coastal and Shelf Science*, *95*(1), 88–98. https://doi.org/10.1016/j.ecss.2011.08.011

Tapia-Silva, F. O., Itzerott, S., Foerster, S., Kuhlmann, B., & Kreibich, H. (2011). Estimation of flood losses to agricultural crops using remote sensing. *Physics and Chemistry of the Earth*, *36*(7–8), 253–265. https://doi.org/10.1016/j.pce.2011.03.005

Tsyganskaya, V. (2019). *Detection of temporarily flooded vegetation using time series of dual polarised C-band synthetic* *aperture radar data*. *September*.

Tsyganskaya, V., Martinis, S., Marzahn, P., & Ludwig, R. (2018a). Detection of temporary flooded vegetation using Sentinel-1 time series data. *Remote Sensing*, *10*(8). https://doi.org/10.3390/rs10081286

Tsyganskaya, V., Martinis, S., Marzahn, P., & Ludwig, R. (2018b). SAR-based detection of flooded vegetation–a review of characteristics and approaches. In *International Journal of Remote Sensing* (Vol. 39, Issue 8, pp. 2255–2293). Taylor & Francis. https://doi.org/10.1080/01431161.2017.1420938

Valipour, M. (2014). Drainage, waterlogging, and salinity. In *Archives of Agronomy and Soil Science* (Vol. 60, Issue 12, pp. 1625–1640). Taylor & Francis. https://doi.org/10.1080/03650340.2014.905676

Van Leeuwen, B., & Tobak, Z. (2015). Operational identification of inland excess water floods using satellite imagery. *GI_Forum 2014 – Geospatial Innovation for Society*, 12–15. https://doi.org/10.1553/giscience2014s12

Van Leeuwen, B., Tobak, Z., & Kovács, F. (2020). Sentinel-1 and-2 based near real time inland excess water mapping for optimized water management. *Sustainability (Switzerland)*, *12*(7), 2854. https://doi.org/10.3390/su12072854

Van Leeuwen, B., Tobak, Z., Kovács, F., & Sipos, G. (2017). Towards a continuous inland excess water flood monitoring system based on remote sensing data. *Journal of Environmental Geography*, *10*(3–4), 9–15. https://doi.org/10.1515/jengeo-2017-0008

Veloso, A., Mermoz, S., Bouvet, A., Le Toan, T., Planells, M., Dejoux, J. F., & Ceschia, E. (2017a). Understanding the temporal behavior of crops using Sentinel-1 and Sentinel-2-like data for agricultural applications. *Remote Sensing of Environment*, *199*, 415–426. https://doi.org/10.1016/J.RSE.2017.07.015

Veloso, A., Mermoz, S., Bouvet, A., Le Toan, T., Planells, M., Dejoux, J. F., & Ceschia, E. (2017b). Understanding the temporal behavior of crops using Sentinel-1 and Sentinel-2-like data for agricultural applications. *Remote Sensing of Environment*, *199*, 415–426. https://doi.org/10.1016/J.RSE.2017.07.015

Vízűgy. (2011). *Information on the 2010–2011 excess water situation*. http://www.vizugy.hu/print.php?webdokumentumid=280 (in Hungarian))

Vreugdenhil, M., Wagner, W., Bauer-Marschallinger, B., Pfeil, I., Teubner, I., Rüdiger, C., & Strauss, P. (2018). Sensitivity of Sentinel-1 backscatter to vegetation dynamics: an Austrian case study. *Remote Sensing*, *10*(9), 1396. https://doi.org/10.3390/rs10091396

Wang, Y. (2002). Mapping extent of floods: What we have learned and how we can do better. *Natural Hazards Review*, *3*(2), 68–73. https://doi.org/10.1061/(asce)1527-6988(2002)3:2(68)

Wang, Y., Hess, L. L., Filoso, S., & Melack, J. M. (1995). Understanding the radar backscattering from flooded and nonflooded Amazonian forests: Results from canopy backscatter modeling. *Remote Sensing of Environment*, *54*(3), 324–332. https://doi.org/10.1016/0034-4257(95)00140-9

Wardlow, B. D., & Egbert, S. L. (2010). A comparison of MODIS 250-m EVI and NDVI data for crop mapping: A case study for southwest Kansas. *International Journal of Remote Sensing*, *31*(3), 805–830. https://doi.org/10.1080/01431160902897858

Wiseman, G., McNairn, H., Homayouni, S., & Shang, J. (2014). RADARSAT-2 Polarimetric SAR response to crop biomass for agricultural production monitoring. *IEEE Journal of Selected Topics in Applied Earth Observations and Remote Sensing*, *7*(11), 4461–4471. https://doi.org/10.1109/JSTARS.2014.2322311

Woodhouse, I. H. (2006). Introduction to microwave remote sensing (1st ed.). In *Taylor & Francis*. CRC Press. https://doi.org/10.1201/9781315272573

Xiao, F., Li, Y. Z., Du, Y., Ling, F., Yan, Y., Feng, Q., & Ban, X. (2014). Monitoring perennial sub-surface waterlogged croplands based on MODIS in jianghan plain, middle reaches of the yangtze river. *Journal of Integrative Agriculture*, *13*(8), 1791–1801. https://doi.org/10.1016/S2095-3119(13)60563-8

Yu, G., Di, L., Zhang, B., Shao, Y., Shrestha, R., & Kang, L. (2013). Remote-sensing-based flood damage estimation using crop condition profiles. *2013 2nd International Conference on Agro-Geoinformatics: Information for Sustainable Agriculture, Agro-Geoinformatics 2013*, 205–210. https://doi.org/10.1109/Argo-Geoinformatics.2013.6621908

Yu, Y., Saatchi, S., Baghdadi, N., & Thenkabail, P. S. (2016). Sensitivity of L-Band SAR backscatter to aboveground biomass of global forests. *Remote Sensing 2016, Vol. 8, Page 522*, *8*(6), 522. https://doi.org/10.3390/RS8060522

Yun, Q. (2017). Ponding excess water mapping in agricultural areas in Hungary. *Universtiy of Twente, Faculty of Geoinformation Science and Earth Observation.* http://essay.utwente.nl/83327/

Zhang, J., Dong, W., Fu, C., & Wu, L. (2003). The influence of vegetation cover on summer precipitation in China: A statistical analysis of NDVI and climate data. *Advances in Atmospheric Sciences 2003 20:6*, *20*(6), 1002–1006. https://doi.org/10.1007/BF02915523

Zhang, M., Li, Z., Tian, B., Zhou, J., & Tang, P. (2016). The backscattering characteristics of wetland vegetation and water-level changes detection using multi-mode SAR: A case study. *International Journal of Applied Earth Observation and Geoinformation*, *45*, 1–13. https://doi.org/10.1016/J.JAG.2015.10.001

APPENDIX

Annex A: Time series of S1 σ^0_{VH} and σ^0_{VV} in WL and NWL area in different wheat fields.

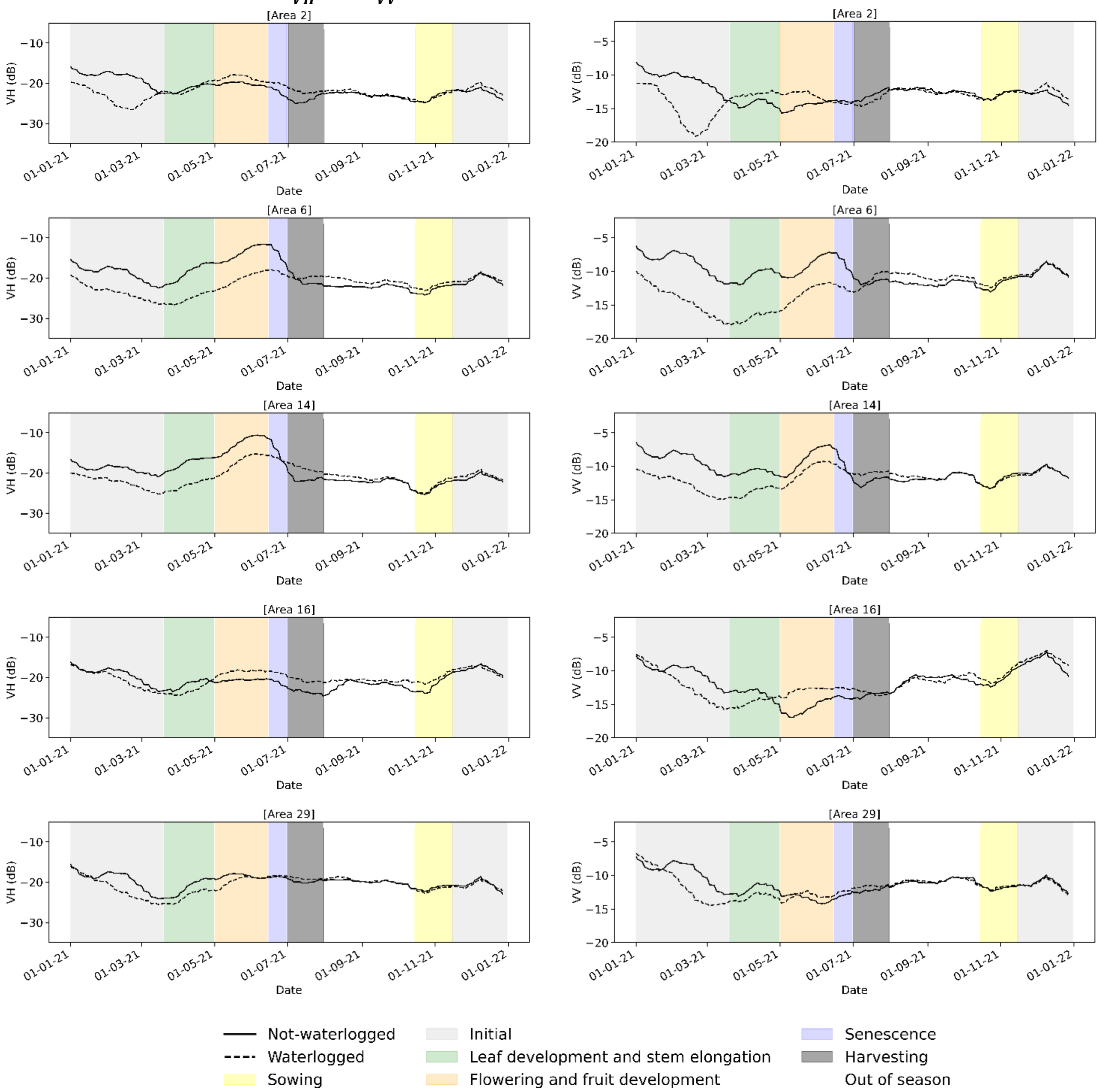

Annex B: Mean NDVI values at the NWL locations in different growth stages

Area id	Leaf development and stem elongation (9th April 2021)	Flowering and fruit development 21st May 2021	Senescence (23rd June 2021)
2	0.71	0.79	0.35
6	0.67	0.86	0.66
14	0.76	0.83	0.47
16	0.53	0.83	0.69
26	0.42	0.83	0.63
27	0.43	0.79	0.52
29	0.46	0.75	0.59

Annex C: Building layer of the test area around Szarvas, Hungary